Remote Sensing of Environment 240 (2020) 111680

Contents lists available at ScienceDirect

Remote Sensing of Environment

journal homepage: www.elsevier.com/locate/rse

Soil moisture experiment in the Luan River supporting new satellite mission opportunities

Tianjie Zhao[a], Jiancheng Shi[a,*], Liqing Lv[b], Hongxin Xu[b], Deqing Chen[c], Qian Cui[c], Thomas J. Jackson[d], Guangjian Yan[e], Li Jia[a], Liangfu Chen[a], Kai Zhao[f], Xingming Zheng[f], Limin Zhao[a], Chaolei Zheng[a], Dabin Ji[a], Chuan Xiong[g], Tianxing Wang[a], Rui Li[a], Jinmei Pan[a], Jianguang Wen[a], Chao Yu[a], Yaomin Zheng[a], Lingmei Jiang[e], Linna Chai[e], Hui Lu[h], Panpan Yao[h], Jianwei Ma[i], Haishen Lv[j], Jianjun Wu[e], Wei Zhao[k], Na Yang[l], Peng Guo[m], Yuxia Li[n], Lu Hu[a], Deyuan Geng[a], Ziqian Zhang[o]

[a] State Key Laboratory of Remote Sensing Science, Aerospace Information Research Institute, Chinese Academy of Sciences, China
[b] Shanghai Academy of Spaceflight Technology, China
[c] Information Center of Ministry of Water Resources of China, China
[d] USDA-ARS Hydrology and Remote Sensing Laboratory (Retired), United States of America
[e] Faculty of Geographical Science, Beijing Normal University, China
[f] Northeast Institute of Geography and Agroecology, Chinese Academy of Sciences, China
[g] Faculty of Geosciences and Environmental Engineering, Southwest Jiaotong University, China
[h] Department of Earth System Science, Tsinghua University, China
[i] China Institute of Water Resources and Hydropower Research, China
[j] College of Hydrology and Water Resources, Hohai University, China
[k] Institute of Mountain Hazards and Environment, Chinese Academy of Sciences & Ministry of Water Conservancy, China
[l] School of Surveying and Land Information Engineering, Henan Polytechnic University, China
[m] College of Information Science and Engineering, Shandong Agricultural University, China
[n] School of Automation Engineering, University of Electronic Science and Technology of China, China
[o] Northwest Institute of Eco-Environment and Resources, Chinese Academy of Sciences, China

ARTICLE INFO

Keywords:
Terrestrial Water Resources Satellite
Soil moisture
Airborne experiment
L-band active and passive
Luan River

ABSTRACT

The Soil Moisture Experiment in the Luan River (SMELR) was conducted from 2017 to 2018 in the semi-arid Luan River watershed located in the North of China. One of the objectives of SMELR is to serve as an assessment tool and demonstration for a new Terrestrial Water Resources Satellite (TWRS) concept with one-dimensional synthetic aperture microwave techniques, for which soil moisture retrieval under variable satellite observing configurations (mainly in terms of incidence angels) is the greatest challenge. This proposed mission is targeted to provide continuity for the current satellite L-band microwave observations, and further improve the accuracy and spatial resolution of soil moisture mapping through the synergistic use of active, passive and optical remote sensing data. Multi-resolution, multi-angle and multi-spectral airborne data were obtained four times over a 70 km by 12 km area in the Shandian River basin, and one time over a 165 km by 5 km area that includes the Xiaoluan River basin. The near surface soil moisture (0 cm–5 cm) was measured extensively on the ground in fifty 1 km by 2 km quadrats (targeted to compare with the airborne radiometer), and two hundred and fifty 200 m by 200 m quadrats corresponding to radar observations. Two networks were established for continuous measurement of the soil moisture and temperature profile (3 cm, 5 cm, 10 cm, 20 cm, 50 cm) and precipitation in the Shandian and Xiaoluan River basin, respectively. Supporting ground measurements also included ground temperature, vegetation water content, surface roughness, continuous measurement of microwave emission and backscatter at a pasture site, reflectance of various land cover types, evapotranspiration and aerosol observations. Preliminary results within the experimental area indicate that (1) the near surface soil moisture spatial variability at a 200 m scale was up to ~0.1 cm^3/cm^3 at an intermediate value of ~0.35 cm^3/cm^3. (2) The difference of soil and vegetation temperature in grass and croplands reach its maximum of 11 K around solar noon time, and the soil temperature gradient is largest at around 15 P.M. (3) Both the airborne and ground

* Corresponding author at: State Key Laboratory of Remote Sensing Science, Aerospace Information Research Institute, Chinese Academy of Sciences, No. 20 Datun Road, Beijing 100101, China.
E-mail address: shijc@radi.ac.cn (J. Shi).

https://doi.org/10.1016/j.rse.2020.111680
Received 19 August 2019; Received in revised form 26 November 2019; Accepted 23 January 2020

measurements cover a wide range of conditions. The L-band active and passive observations exhibit a large variation of ~30 dB and ~80 K, respectively, corresponding to soil moisture range from 0.1 cm^3/cm^3 to 0.5 cm^3/cm^3. The sensitivity of both active and passive data to soil moisture is compared at corresponding spatial resolutions and show high information complementarity for better accuracy and resolution soil moisture retrieval.

1. Introduction

As a key parameter in hydrological cycle, soil moisture plays an important role in the hydrological processes such as infiltration, runoff and evapotranspiration (Seneviratne et al., 2010; Corradini, 2014; Brocca et al., 2017). It is also a direct indicator for flood and drought monitoring and serves as a critical variable in flood modelling and drought assessment (Bonan and Stillwell-soller, 1998; Saini et al., 2016). Soil moisture is the basis water resource that affects the growth and development of terrestrial vegetation, and hence, its temporal-spatial distribution is required for irrigation management and agriculture production. Soil moisture governs the partitioning of the water, energy and carbon exchanges between the land-atmosphere (De Rosnay et al., 2009). The establishment of an effective global soil moisture observation system for Earth system science research and related applications has become a common goal of scientists.

Traditionally, ground-based soil moisture can be measured by the gravimetric method, which is still widely used as it is the only direct (accurate) way of measuring soil moisture. But it generally can only represent a small space range, and it is time-consuming and laborious. The usage of Time Domain Reflectometry (TDR) and Frequency Domain Reflectometry (FDR) sensors has become a new standard approach to measure soil moisture (Topp, 1980; Bogena et al., 2017), as they were found to be accurate for a wide range of soil types and less time-consuming. By utilizing wireless networks, it is possible to use ground-based systems to measure soil moisture for larger areas such as a watershed scale (Robinson et al., 2008). In the last decades, cosmic ray neutron systems (Franz et al., 2012) have been used to provide soil moisture measurements over a much larger scale, but its usage and representativeness still requires further investigations. However, at this time none of these methods can provide soil moisture information at a global scale.

Remote sensing technology, especially the development of microwave remote sensing, has made it possible to measure and monitor soil moisture over large areas. With the launch of the SMOS (Soil Moisture and Ocean Salinity, Kerr et al., 2010) and SMAP (Soil Moisture Active Passive, Entekhabi et al., 2010) satellites, L-band radiometry from space have become the most effective means of measuring soil moisture at the global scale (Wigneron et al., 2003; Wigneron et al., 2017). The development of those missions depended not only on the advances of microwave instruments and related physical models, but also on the demonstration of the new technologies and validation of retrieval concepts using airborne and ground-based experimental research. These experiments have also played a significant role in promoting the development of remote sensing, soil science, hydrology and other related disciplines to address a very broad science questions beyond soil moisture, and it is pivotal for calibration/validation studies before and after the mission launch.

The earliest longer term/larger domain airborne experiments date back to the 1980s. The Hydrologic Atmospheric Pilot EXperiment (HAPEX) was conducted in 1986 in Southwestern France to measure the hydrological budget and evaporation flux at the climatic scale (Nichols et al., 1993). This was followed by the First ISLSCP (International Satellite Land Surface Climatology Project) Field Experiment (FIFE) conducted over the Konza Prairie in Kansas, from the summer of 1987 to 1989 (Wang et al., 1990). In those two experiments, an L-band Pushbroom Microwave Radiometer (PBMR) was used to collect the brightness temperature, which is found to correspond to spatial and temporal soil moisture variation. The MACHYDRO'90 is a Multi-sensor Aircraft Campaign for Hydrology, Synthetic-aperture radar (SAR) measurements were conducted together with passive microwave from PBMR to explore the synergistic use of microwave sensors (Jackson et al., 1994). Together with the Monsoon'90 multidisciplinary field campaign (Kustas and Goodrich, 1994), scientists in the 1980s attempted to understand the reliability of microwave remote sensing in monitoring soil moisture over a wide range of ground conditions (Schmugge et al., 1992).

A milestone was achieved in Monsoon'91 and Washita'92, the major contribution of which is that it utilized the Electronically Scanned Thinned Array Radiometer (ESTAR) to map soil moisture at high resolution. These experiments verified that the concept of aperture synthesis microwave radiometry using the ESTAR instrument could be employed as a soil moisture sensor in the Walnut Gulch and Little Washita watersheds (Jackson et al., 1993; Jackson et al., 1995). The Space Shuttle Imaging radar mission (SIR—C) was implemented to map soil moisture in bare soil in Washita'94 (Wang et al., 1997; Shi et al., 1997). The airborne remote sensing data and measured ground data collected in the Washita experiments were used to study the hydrological process and provided a data basis for verifying the accuracy of SSM/I (Special Sensor Microwave Imager) soil moisture (Jackson, 1997). The SGP (Southern Great Plains in 1997 and 1999) experiments focused on how to effectively use less than optimal sources of satellite microwave data for soil moisture mapping and supported the algorithm development of the AMSR-E (Advanced Microwave Scanning Radiometer-EOS) soil moisture inversion. Another milestone of SGP'99 is that the Passive and Active L-band System (PALS), which is a prototype of the Aquarius and SMAP mission, was first used in the airborne experiment (Jackson et al., 1999; Jackson and Hsu, 2001). These experiments during the 1990s gave rise to the two important soil moisture missions of SMOS and SMAP.

The SMEX (Soil Moisture Experiment) aimed to implement and develop global soil moisture observation systems available at the time, especially to validate the AMSR-E brightness temperature and soil moisture retrievals (Narayan et al., 2004; Jackson et al., 2005; Bindlish et al., 2006; Bindlish et al., 2008; Cosh et al., 2009). The scientific questions of SMEX include how to upscale soil moisture observations to watershed and satellite footprint scales, and how to retrieve soil moisture under different soil and vegetation types, that is, using satellite observations to distinguish vegetation and soil information. These objectives led to the requirements for detailed ground sampling, high-resolution airborne observations concurrent with satellite overpasses, and conversion between different scales from the ground, aircraft and satellite. The United States Department of Agriculture (USDA) and National Aeronautics and Space Administration (NASA) collaborated on the SMEX for four consecutive years (2002–2005) in the Walnut River, Litter River, Walnut Gulch, Walnut Creek and other watersheds in the United States, covering a variety of typical surface vegetation cover types and Soil condition. The airborne data were collected with various instruments including the PSR (Polarimetric Scanning Radiometer), ESTAR, PALS, and a new instrument 2DSTAR (2-Dimensional Scanned Thinned Array Radiometer). These experiments and associated research went well beyond the development of various soil moisture retrieval algorithms (Njoku et al., 2003; Njoku and Chan, 2006; Paloscia et al., 2006; Owe et al., 2008; Li et al., 2010) and validation of several satellite soil moisture products (Cosh et al., 2006; Jackson et al., 2010; Jackson et al., 2012).

The EuroSTARRS (Salinity Temperature and Roughness Remote Scanner) campaign was designed to support the processing scheme

before the launch of the SMOS mission, which obtains multi-angular brightness temperature at L-band (Saleh et al., 2004). The NAFE (National Airborne Field Experiment) in 2005 and 2006 was a large-scale soil moisture remote sensing experiment conducted by the University of Melbourne, Australia (Panciera et al., 2008; Merlin et al., 2008). It provided a wide range of PLMR (Polarimetric L-band Multibeam Radiometer) airborne data and ground-based monitoring data, which supported studies of the SMOS soil moisture algorithms, and 1-km resolution soil moisture by combining passive microwave and optical data.

In 2007, 2008 and 2009, three airborne campaigns involving 21 flights were carried out over Southwest France, the Valencia site and the Bay of Biscay to obtain the bi-angular observations at L-band, in which the RFI were detected (Zribi et al., 2011; Pardé et al., 2011a). The first testing of the 2-Parameter inversion algorithm was conducted based on the L-MEB (Wigneron et al., 2007), which is a component of the SMOS algorithm (Pardé et al., 2011b). Following the launch of SMOS mission, the AACES filed experiment was conducted in 2010 to provide a comprehensive assessment of SMOS data across the Murrumbidgee River catchment in Australia (Peischl et al., 2012). Those experiments provided important insights into key issues of the SMOS mission such as brightness temperature reconstruction and RFI detection, parameter retrievals with the feature of multi-angular ability and calibration, validation and application of the SMOS data.

As the SMAP soil moisture mission evolved, a series of soil moisture experiments were conducted. The main supporting field campaigns, before the launch of SMAP, include the Canadian Experiment – Soil Moisture 2010 (CanEx-SM10), the Soil Moisture Active and Passive Experiments (SMAPEx) and SMAPVEX12 (Magagi et al., 2013; Panciera et al., 2014; McNairn et al., 2015). The main airborne instruments include PALS, PLMR and UAVSAR, which were used to collect microwave active/passive observations covering a wide range of vegetation types and soil moisture conditions in different geographic regions (USA, Canada and Australia). These datasets provided a means to test and improve models and algorithms used for SMAP soil moisture retrieval. The post-launch field campaigns of SMAPVEX in 2015 and 2016 (Colliander et al., 2017) were conducted in support of the quality assessment of SMAP products and their improvement and applications, especially over the targeted core validation sites. It is worth noting that the root-zoon soil moisture was measured with the Airborne Microwave Observatory of Subcanopy and Subsurface (AirMOSS) radar instrument (Tabatabaeenejad et al., 2015), which might be a new opportunity of Earth explorer from space.

There have also been a few airborne experiments conducted in China. One of the successful examples is the Watershed Allied Telemetry Experiment Research (WATER) and its successor of Heihe Watershed Allied Telemetry Experiment Research (HiWATER), which were mainly focused on the understanding of the hydrological and ecological processes at a catchment scale (Li et al., 2009; Li et al., 2013). Soil moisture retrievals were attempted (Zhang et al., 2015), and those are designed toward application of remote sensing in ecohydrology studies but not satellite mission development.

From the review presented above (summarized in Table 1, Jackson et al., 2016), one can see that filed experiments have played a significant role in soil moisture mission development and its calibration and validation activities. Most soil moisture experiments conducted focused on L-band radiometry, since it is the optimal operational band for soil moisture retrieval (Kerr et al., 2012; Al-Yaari et al., 2019) and a useful tool for monitoring vegetation dynamics and carbon stocks (Fan et al., 2019; Li et al., 2020). With the great success of the SMOS and SMAP missions, scientists are seeking continuity of L-band observations from space, especially with a more enhanced spatial resolution. Two possible new opportunities are being considered by China, including the Water Cycle Observation Mission (WCOM, Shi et al., 2014) and the Terrestrial Water Resources Satellite (TWRS) (it has not been finally approved by the State Administration for Science, Technology and Industry for National Defense). Unlike the SMOS and SMAP, the WCOM and TWRS are both based on the one-dimensional (1-D) synthetic aperture technology, which can reduce the complexity as compared with two-dimensional (2-D) radiometer of SMOS. It can also avoid the risk of large antenna rotating (SMAP) to obtain high resolution observations in the cross-track direction. Except the 1-D radiometer at L-band, a synthetic aperture radar at L-band is designed to share the reflector antenna. Optical instruments including a multi-angular thermal infrared camera, multispectral and hyperspectral imagers are being evaluated to monitor other elements of water resources such as

Table 1
The soil moisture experiments heritage.

Name	Year	Location	Microwave instruments	References
HAPEX	1986	Toulouse, France	PBMR	Nichols et al., 1993
FIFE	1987–1989	Konza Prairie in Kansas, USA	PBMR	Wang et al., 1990
MACHYDRO	1990	Mahantango Creek in Pennsylvania, USA	PBMR, AirSAR	Jackson et al., 1994
Monsoon	1990	Walnut Gulch in Arizona, USA	PBMR	Kustas and Goodrich, 1994
Monsoon	1991	Walnut Gulch in Arizona, USA	ESTAR	Jackson et al., 1993
Washita	1992	Little Washita in Oklahoma, USA	ESTAR, AirSAR	Jackson et al., 1995
Washita	1994	Little Washita in Oklahoma, USA	SIR-C, ESTAR	Wang et al., 1997; Shi et al., 1997
SGP	1997	Little Washita in Oklahoma, USA	PSR, ESTAR	Jackson et al., 1999
SGP	1999	Little Washita in Oklahoma, USA	PSR, PALS, ESTAR	Jackson and Hsu, 2001
EuroSTARRS	2001	France and Spain	STARRS	Saleh et al., 2004
SMEX	2002	Iowa, USA	PSR, PALS, ESTAR, AirSAR	Narayan et al., 2004; Bindlish et al., 2006
SMEX	2003	Alabama, Georgia, Oklahoma, USA	PSR, 2DSTAR, AirSAR	Jackson et al., 2005
SMEX	2004	Arizona, Sonora, USA	PSR, 2DSTAR	Bindlish et al., 2008
SMEX	2005	Iowa, USA	APMIR	Cosh et al., 2009
NAFE	2005	Australia	PLMR, EMIRAD	Panciera et al., 2008
NAFE	2006	Australia	PLMR	Merlin et al., 2008
CLASIC	2007	Oklahoma, USA	PSR, PALS	Miller et al., 2007; Bindlish et al., 2009
CAROLS	2007–2009	France and Spain	CAROLS	Pardé et al., 2011a; Pardé et al., 2011b
WATER	2007–2009	Heihe, China	Chinese radiometer	Li et al., 2009
AACES	2010	Murrumbidgee River catchment, Australia	PLMR	Peischl et al., 2012
CanEx-SM10	2010	Saskatoon, Saskatchewan, Canada	Canadian radiometer, UAVSAR	Magagi et al., 2013
SMAPEx1-5	2010–2011	New South Wales, Australia	PLMR, PLIS	Panciera et al., 2014
HiWATER	2012–2015	Heihe, China	PLMR, Chinese Radiometer	Li et al., 2013
SMAPVEX	2012	Manitoba, Canada	PALS, UAVSAR	McNairn et al., 2015
SMAPVEX	2015	Arizona, USA	Upgraded PALS, UAVSAR, AirMOSS	Colliander et al., 2017
SMAPVEX	2016	Iowa, USA and Manitoba, Canada	Upgraded PALS	McNairn et al., 2016

dynamic changes of water, water environment and quality, wetlands, snow and ice etc. As the main payload for soil moisture, the issues with 1-D radiometer is that the incidence angle can be different for every satellite overpass. This leads to the requirement of accurate correction of angular effects from both vegetation and roughness. The SMAP mission has demonstrated that the downscaling of brightness temperature can be achieved based on radar observations at the same incidence angle of 40°. Is the relationship still robust if active and passive observations were made at different angles? The hyperspectral observations can predict well the vegetation biophysical parameters, and the multi-angular infrared observations can separate the vegetation and soil temperature. How can this ancillary information improve the soil moisture retrievals in terms of accuracy and resolution? Therefore, to further understand those issues, a Soil Moisture Experiment in the Luan River (SMELR) was designed and conducted to support the demonstration of the TWRS. The selection of Luan River is because this region is less affected by the Radio Frequency Interference (RFI) in China. And it contains various land cover types such as croplands, grasslands, shrublands and forests with topography effects in support of evaluation of mission requirements.

In this paper, we present the first active-passive microwave and optical synergistic observation airborne experiment in China, toward the demonstration of the future Chinese TWRS and requirements of regional water resources management. The first part of this paper describes the experimental area and scientific objectives. Main compositions of this experiment including the airborne missions, ground sampling strategies, ground-based observation experiments and soil moisture measurement through wireless sensor networks are introduced in the second part. The third part gives the initial results of active and passive microwave data, variations of the ground data and their relationships.

2. Overview of SMELR

With the requirements of mission development of the TWRS, and the research needs of regional water resources management, a space-air-ground integrated experiment of soil moisture was conducted in the Luan River of China. Soil moisture will be examined from different spatial scales including existing satellites, airborne observations and instantaneous and long-term ground sampling as shown in Fig. 1. The airborne instruments are selected according to the configuration of the TWRS. It was the first active-passive microwave + optics synergistic observation airborne experiment in China. The L-band active-passive synergistic observations were made at different angles, which is unprecedented in previous experiment.

2.1. Experimental area description

The Luan River is the second largest river in the North China region. It originates in northern Hebei, where its headstream is called as the Shandian River. It flows northwards into the province of Inner Mongolia, and then flows southeast back into Hebei, where it is joined by its tributary of the Xiaoluan River. The Luan River finally discharges into the Bohai Sea. It is 877 km long and flows through an area of 44, 600 km^2. It is an important water source for the Beijing-Tianjin-Hebei region, as well as a water conservation and ecological function zone. The Luan River has a large inter-annual variation of runoff, which mainly comes from rainfall. Therefore, the annual distribution of runoff and precipitation during the year has great consistency. The flood season starts from the end of June to the beginning of September, and the amount of flow in winter and spring is very small. In March and April, melting snow often leads to a small spring flood. The experimental area has a temperate continental climate, and the average annual precipitation in most areas is 300–500 mm, 70% of which is concentrated in July to September. During September 2018, the average regional precipitation is ~8.2 mm/month as detected by a precipitation network (19 sites available), and the precipitation events (rainfall rates exceeding 0.2 mm/h) happened on Sep. 1st (1.51 mm), Sep. 11th (1.95 mm), Sep. 25th (1.64 mm), and Sep. 27th, 2018 (1.46 mm).

The experimental area (See Fig. 2) covers an area of 2° × 2° (41–43°N; 115.5–117.5°E) in the upper stream of the Luan River that includes the relatively flat Shandian River basin and the Xiaoluan River basin with complex terrain. The land cover of the study area is mainly grassland, croplands, forest, a small number of shrublands and bare ground. Therefore, the airborne flights are designed to span areas with croplands, grasslands and forests. Intensive and long-term ground observation experiments are conducted within the Shandian River basin and the Xiaoluan River basin as core experimental areas.

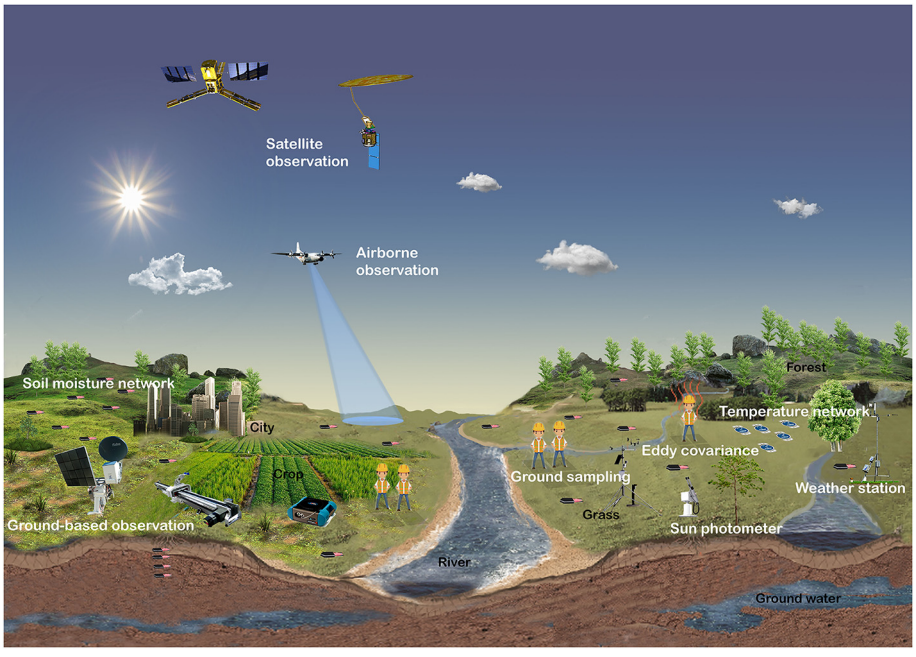

Fig. 1. Overview of the SMELR design.

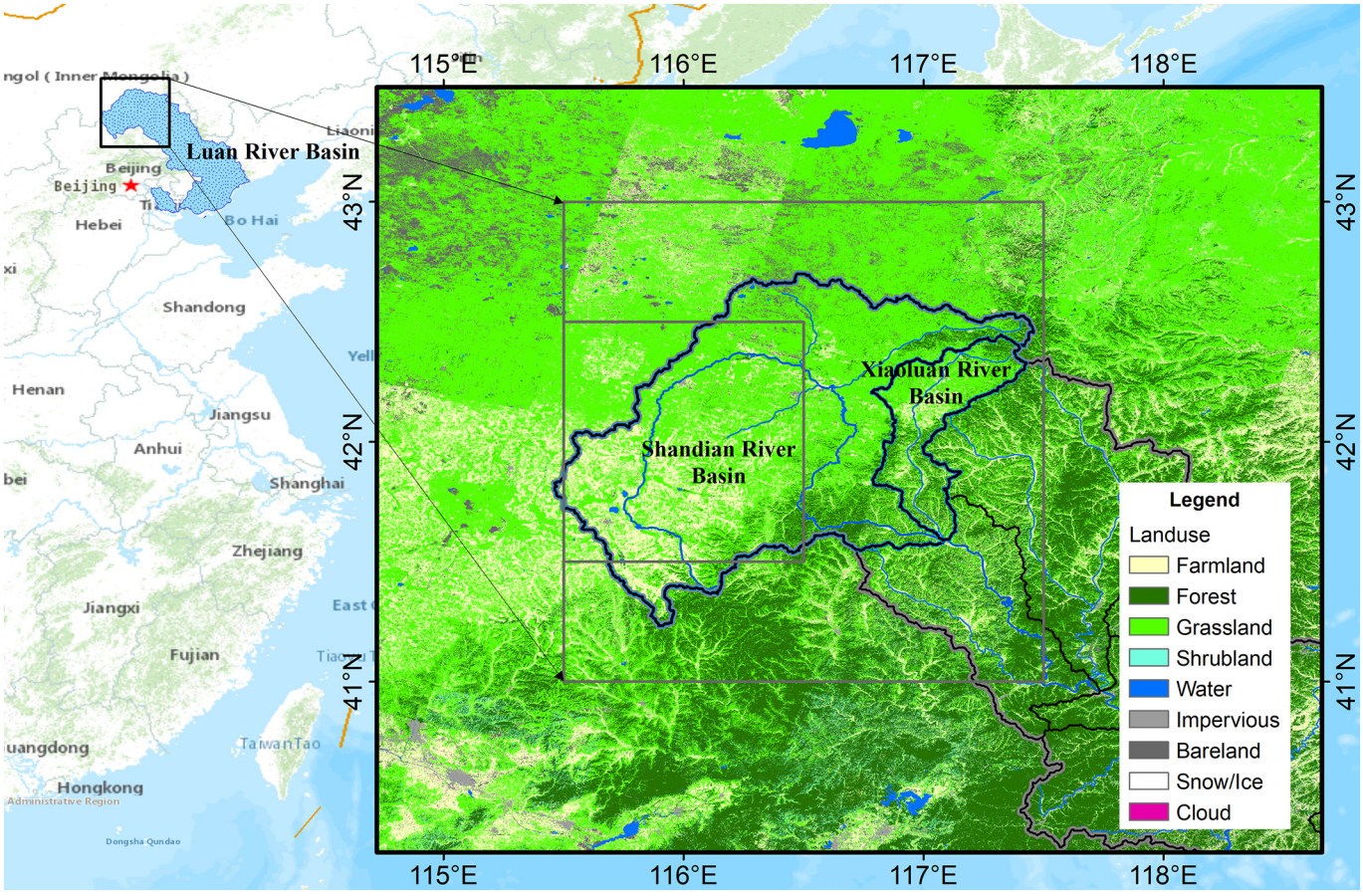

Fig. 2. Experimental areas of the SMELR.

Table 2
Summary of the experiment composition.

Composition	Tasks	Variables/parameters	Methodologies/instruments
Airborne experiments	Airborne microwave remote sensing	Brightness temperature, backscatter coefficient	L-band active-passive microwave sensor
	Airborne optical remote sensing	Radiation brightness	Optical imaging system including infrared, multispectral and hyperspectral cameras
Ground sampling campaign	Ground sampling of soil moisture	Soil moisture at 0–5 cm, 10 cm, 20 cm, and 40 cm	FDR (Delta-T ML3), thermogravimetric method
	Ground sampling of surface temperature	Temperature of shaded soil, illuminated soil, 5-cm soil, shaded and illuminated vegetation	Thermistor of TR-52i, HOBO MX2201 temperature logger
	Vegetation parameter measurement	Vegetation water content, LAI/NDVI, vegetation structure parameters	Destructive sampling method, LAI−2200C, ASD field spectroradiometer, ruler and protractor
	Surface roughness measurement	Root mean squared height, correlation length	Needle board
	Survey of lake and reservoir	Water temperature and salinity, wind speed and direction, nitrogen, phosphorus and chlorophyll in water	Conductivity and salinity meter (EC450), HOBO MX2201 temperature logger, anemometer
Ground-based measurements	Ground-based microwave observation in 2017	Brightness temperature	Ground-based radiometer (RPG-6CH-DP)
	Ground-based microwave observation in 2018	Brightness temperature, backscatter coefficient	Ground-based radiometer (RPG-6CH-DP) and radar (GB-SAR)
	Spectral field measurements	Radiation brightness, reflectance	ASD field spectroradiometer
	Atmospheric parameter observation	Atmospheric optical thickness	CE318 Sun photometer
Long-term ground observations	Soil moisture, temperature and precipitation network	Soil moisture and temperature at 3 cm, 5 cm, 10 cm, 20 cm and 50 cm, rainfall rate	Decagon 5TM, HOBO rain gauge
	Flux measurement system	Carbon dioxide, water vapor and energy fluxes, soil heat flux and temperature, air temperature and humidity etc.	Closed-Path Eddy-Covariance system of CPEC200, HFP01 heat flux sensor, HMP155 humidity and temperature probe etc.
	Surface radiation observation system	Four-component radiation, meteorological parameters	Four-component radiometer MR-60, WS601 weather sensors

Table 3
Configuration of the L-band active-passive microwave sensor.

	Radiometer	Radar
Central frequency	1.41 GHz	1.26 GHz
Bandwidth	24 MHz	5 MHz
Polarization	H, V	HH, VV, HV, VH
Incidence angle	20°–34° (Mechanically scanning)	33°–63° (Electronically scanning)
−3 dB beam width	18°	30°
Ground resolution	1–1.4 km (3000 m height)	50–180 m (3000 m height)
Accuracy	Uncertainty ≤1.8 K	Noise equivalent ≤ −30 dB

2.2. Scientific objectives

As soil moisture is a key boundary condition in the land surface processes and its exchanges with atmosphere, it is identified as a primary parameter that needs to be observed by the Chinese TWRS. The experiment was designed to explore several scientific and technical questions that include:

1. What are the mission minimum requirements for the scientific measurements and instrument performance?
2. How to perform accurate correction of angular effects from both vegetation and roughness, and better retrieve soil moisture with L-band active-passive observations at varying incidence angles? How to obtain a higher spatial resolution soil moisture through the combining use of radar and optical data?
3. What is the impact of the temperature difference between vegetation and soil (caused by the afternoon orbit) on the soil moisture retrieval? Does the surface component temperature obtained by the infrared observations help to improve the accuracy?
4. Toward the validation of soil moisture satellite products, how can soil moisture be measured more accurately at different spatial scales, and how to design the observation schemes and upscaling strategies especially for large-scale heterogeneous surface?
5. How can soil moisture improve the hydrological modelling, drought prediction and flood forecasting toward water resources management in the Luan River, and how does it influence the land-atmosphere exchanges of water and energy, such as the evapotranspiration?

Therefore, the specific objectives of this experiment are:

1. Mission requirements identify through experimental data and model simulations;
2. To develop and validate microwave scattering/emission models and active/passive soil moisture retrieval algorithms to fulfill the mission objectives;
3. To improve the accuracy and spatial resolution of soil moisture products through the synergistic use of multi-source remote sensed data, especially the treatment of vegetation and ground temperature;
4. To establish a multiscale soil moisture monitoring network in the Luan River in support of studies on scale conversions as an in-situ calibration/validation site;
5. To produce various high-quality remote sensing products to support the estimation of evapotranspiration, and further improve the application potential of remote sensing in hydrological modelling and water resources management.

3. Experiment composition

The SMELR is composed of airborne experiments, ground sampling campaign, ground-based measurements and long-term observations. Table 2 summarizes the experiment composition.

3.1. Airborne experiments

The SMELR aircraft flights were carried out by the Chinese Yunshuji-8 (Y-8) produced by Shaanxi Aircraft Corporation. The Y-8 was equipped with an instrumentation pod under the left-hand wing, where airborne instruments were installed in two separate containers for microwave and optical sensors, respectively. The flight speed was designed to be in the range of 400 km/h–450 km/h to ensure a high repetition rate of optical observations. The relative altitude of flight was 3000 ± 200 m, and the flight attitude accuracy was controlled within the range of ± 3° for all the roll angle, pitch angle and yaw angle.

3.1.1. Airborne instruments

The airborne instruments include an L-band active-passive microwave sensor developed by the Shanghai Academy of Spaceflight Technology, and an optical imaging system including multispectral, hyperspectral and thermal infrared observations developed by the Aerospace Information Research Institute.

The microwave sensor (Table 3) contains an L-band radiometer, which scans at a constant speed across the flight direction. Radiometric data were collected within a small range of incidence angle (20° to 34°) with a spatial resolution from 1 to 1.4 km. The L-band radar provides a spatial coverage of about 2 km, which approximates those of the scanning radiometer. It collected backscatter data in four linear polarizations (HH, VV, VH, HV) with the incidence angle ranging from 33° (near range) to 63° (far range). The spatial resolution of radar is about one-twelfth of the radiometer's resolution for supporting the study of active-passive downscaling. The optical system (Table 4) can simultaneously obtain multi-spectral, hyperspectral and dual-angle infrared images with a spatial resolution ranging from 2 to 4 m at a relative flight height of 3000 m.

The radiometer was internally calibrated by an internal ambient reference temperature load and a noise diode (hot reference). External targets including the water body (Hulunnao'er as the cold reference) and grasslands (hot reference observed by a ground-based radiometer) were used to perform the second-calibration. The radar calibration was supported by several large size (leg dimension of 2, 3 m) corner reflector with different radar cross section. A calibration site was also selected for reflectance measurements of ground artificial white and black targets to calibrate the absolute radiometric response of the optical imaging system.

3.1.2. Airborne missions

There are two flight regions (Fig. 3). The first one within the Shandian river basin is about 70 km × 12 km, which is designed to cover at least seven grids of 9-km SMAP enhanced products (Chan et al., 2018). In one of those grids, eight sites were selected to perform long-term soil moisture and temperature measurement for representing the average of soil moisture toward SMAP product validation. This whole region is relatively flat and partially covers the dry riverbed of the Shandian river that turned into wetland. The main types of land cover are cropland (south) and grassland (middle north). There were 11 flight

Table 4
Configuration of the optical imaging system.

	Dual-angle infrared camera	Multispectral camera	Hyperspectral camera
Bands	8 μm–12 μm	0.43–0.47 μm 0.52–0.58 μm 0.65–0.71 μm 0.82–0.88 μm	Range: 0.4–1.0 μm 5 nm width 346 bands
Incidence angle	0°, 31°	0°	0°
Swath width	2.5 km	3 km	2.5 km
Ground resolution	4 m (3000 m height)	2.1 m (3000 m height)	2.8 m (3000 m height)

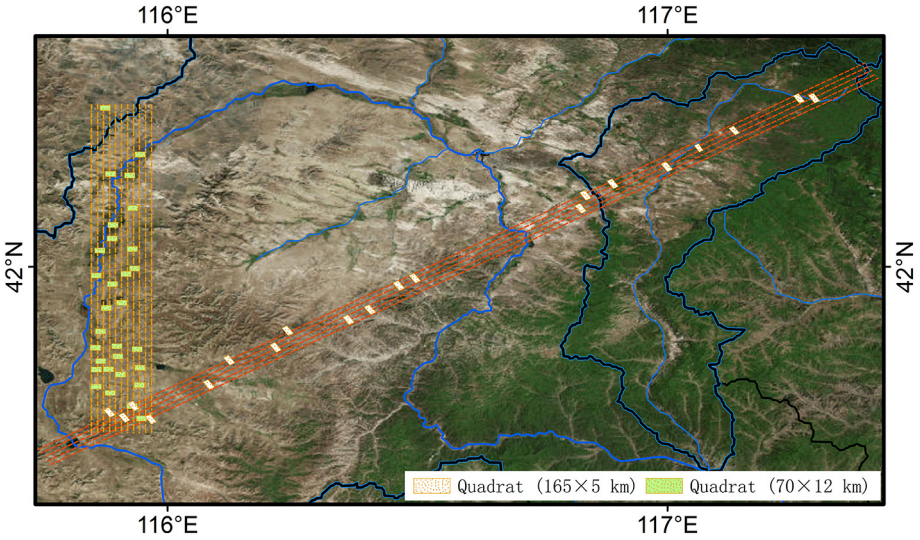

Fig. 3. Flight lines and ground quadrats.

lines with an interval of 1 km to ensure a full coverage capability of each incidence angle (multi-angular observations of land surface). Four flights were completed over this region #1 on Sep. 17th, 19th, 24th, and 26th respectively. The second one covered a 165 km × 5 km domain that starts from the Shandian river basin in the southwest to the Xiaoluan river basin in the northeast, where ground conditions are with complex topography and forests. It covers a soil moisture and temperature network installed in the Xiaoluan river basin. The whole region contains grassland, cropland, shrubland, desert, lakes and plantation. Similarly, there are 5 flight lines with 1 km interval. Airborne experiment was conducted over this region #2 only on Sep. 20th. All airborne missions are summarized in Table 5.

3.2. Ground sampling campaign

In order to match the spatial resolutions of the airborne radiometer and radar, the large quadrat for radiometer is designed to have a sampling area of 1 km × 2 km. 30 and 20 large quadrats were selected in the flight regions of 70 km × 12 km and 165 km × 5 km respectively, as shown in Fig. 3. Sampling personnel were divided into 10 teams, each team consisting of 3–4 people responsible for completing the soil moisture and temperature measurement of 2–3 large quadrats. Because the spatial variability of soil moisture is significant, the large quadrats were distributed into various parts of the flight regions according to the road accessibility, and the sampling of soil moisture within each large quadrat is necessarily dense. The measurement density of temperature could be sparser, but the time of measurement needs to be close to the aircraft transit, because temperature may change rapidly with time.

Within each large quadrat (See Fig. 4), 5 small quadrats (200 m × 200 m corresponding to the resolution of radar) were identified according to the uniformity of land cover. Within each small quadrat, 5 sampling locations were set uniformly, and each location was repeatedly observed 3–6 times using a handheld ML3 Theta Probe Soil Moisture Sensor (accuracy of ± 0.01 cm^3/cm^3). For at least one point, surface temperature was measured with a thermistor (TR-52i with accuracy of 0.1 K) for shaded soil, illuminated soil, 5-cm soil, shaded and illuminated vegetation. Within each large quadrat, one soil sample was collected with a ring cutter for gravimetric soil moisture and bulk density measurements by the oven drying method, which could be used for calibrating the ML3 sensor. Each team dug a pit on each flight day to measure soil moisture and temperature at different depths (5, 10, 20, 40 cm).

As a complementary to temperature measurements within quadrats, which may be limited for time synchronization, HOBO MX2201 waterproof temperature loggers (accuracy of 0.5 K) were used to record the surface temperature continuously from Sep. 13th to 27th. Ten fixed locations including grassland, cropland, woodland, bare soil and pavement were selected to perform the measurement. One team took care of these instruments and measured surface temperature randomly during the flights.

Vegetation water content was measured by a destructive sampling method that cuts the vegetation (0.8 m × 0.8 m) above the soil, measures its fresh weight, dries the sample and measures the dry weight. For crops with distinct stems and leaves, the water content of the vegetation was determined separately. Vegetation samples include grass, corn, potatoes, carrots, buckwheat etc. Soil roughness condition was recorded by taking pictures of a 1-m needle board. For croplands, three measurements were conducted along and perpendicular to the ridge to obtain a soil surface profile of 3 m respectively. For other land covers such as grasslands, measurements were taken similarly for each north-south and east-west direction. Root mean squared height and correlation length were calculated based on the digital 3-m soil profiles. Vegetation water content and soil roughness measurement were conducted within the above designed quadrats by another two teams.

The Hulunnao'er Lake was used as the cold target for in-flight calibration of the L-band microwave radiometer. The Y-8 aircraft was flown as lowest as possible to ensure the radiometer footprint was included within the lake boundary (3.2 km × 2.4 km). During each flight, transects of water temperature and salinity in the top layer were measured. In addition, wind speed and direction were undertaken for an accurate modelling of the lake brightness temperature. Surface water samples were also collected for nitrogen, phosphorus and chlorophyll measurement to support remote sensing of water quality.

3.3. Ground-based measurements

Ground-based microwave observation experiments were conducted

Table 5
Airborne missions.

	Date	Duration	Flight region
1	2018.09.17	13:00–16:30	#1: 70 km × 12 km
2	2018.09.19	08:00–11:30	#1: 70 km × 12 km
3	2018.09.20	12:00–15:30	#2: 165 km × 5 km
4	2018.09.24	10:10–14:10	#1: 70 km × 12 km
5	2018.09.26	10:50–14:20	#1: 70 km × 12 km

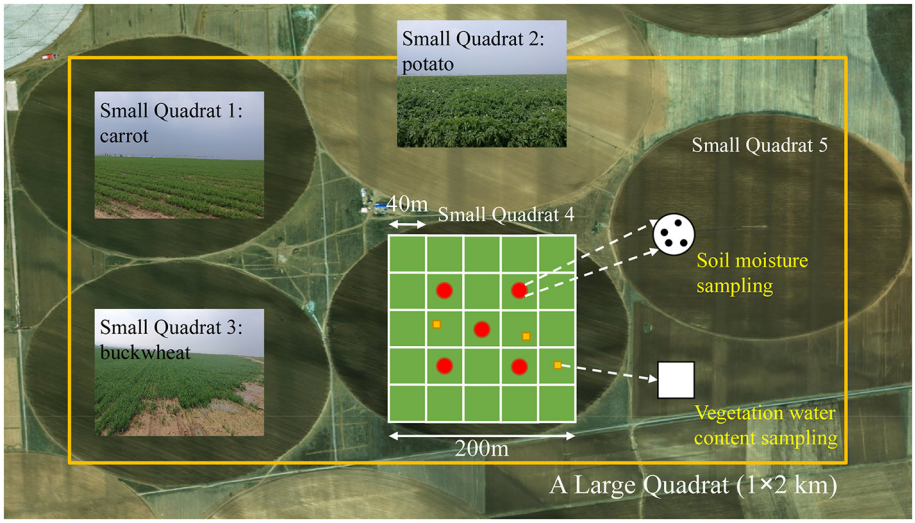

Fig. 4. Ground sampling strategy within a large quadrat (1 km × 2 km).

in 2017 and 2018, respectively for croplands and grasslands. In 2017, the experiment was conducted only with a radiometer in Duolun County, Inner Mongolia (116.47°E, 42.18°N, at 1269 m altitude). Three types of crops (corn, buckwheat and *Avena nuda*) were observed throughout the whole growth stage. The RPG-6CH-DP multi-frequency radiometer was used to measure the polarized brightness temperature at L-band (1.4 GHz), C-band (6.925 GHz), and X-band (10.65 GHz). In 2018, one of the experiment fields (~4 km^2), which is in a pasture (Xinyuan) in Zhenglan Banner, Inner Mongolia (115.93°E, 42.04°N, at 1362 m altitude), was selected to conduct the ground-based measurement of both microwave emission and backscatter. Observations started on Aug. 18th and ended on Sep. 25th, 2018. The elevation angle of the RPG-6CH-DP radiometer was set from −60° to 90° (zenith direction). In order to avoid the influence of surface heterogeneity, the radiometer was set to scan in four directions (azimuth angle). Once the weather is cloudless, the C- band X-bands were calibrated by using the sky-tipping method, and the L-band was calibrated using the two-point calibration method to achieve the absolute system accuracy within 1 K. Radar observations was conducted by using a ground-based SAR (GBSAR). Only one measurement per day was token at L-, C- or X- band in four polarization: VV, VH, HH, HV. Radar calibration was performed using a metal sphere plus any second target with a strong cross polarized radar cross section.

In addition, some important parameters (soil moisture, surface roughness and vegetation properties) were measured simultaneously over the Xinyuan pasture site in 2018. Soil moisture and temperature were simultaneously measured by the Decagon EM50 instrument (5TM probes) every 10 min. The nominal resolution and accuracy of 5TM probe are 0.0008 cm^3/cm^3 (± 0.03 cm^3/cm^3) for soil moisture and 0.1 K (± 1 K) for soil temperature. These probes were installed at the following depth: 0–1 cm, 3 cm, 5 cm and 10 cm. The grass vegetation water content was sampled about every 3 days. The surface roughness parameters were measured by a needle board every week. Those ground-based measurements (Fig. 5), especially the multi-angular observations for both active and passive microwave, were continuously conducted according to the weather condition and can be used for the comparison and calibration with airborne observations and research on active-passive retrieval algorithms.

Another truck-mounted radiometer provided by Northeast Institute of Geography and Agroecology was used to provide mobile measurement at L-band of various ground targets. Water bodies, grassland, corn, potato and carrot fields, and bare agriculture soil were observed during the experimental period. The incidence angle was set to be from 40° to 70° to explore the angular behavior of different ground targets.

Moreover, the ASD field spectroradiometer was used to measure reflectance of various land cover types including soil, grasslands and croplands during the period of experiment. It is aimed to obtain vegetation properties by optical remote sensing and provide complementary and independent information of vegetation for microwave soil moisture retrievals. The vegetation spectrum was measured by the ASD spectroradiometer ranges from 400 nm to 2500 nm. The measurements also include supporting parameters i.e. soil moisture, vegetation water

Fig. 5. Continuous observations of microwave emission and backscatter at a pasture site (Xinyuan).

content, and leaf area index (LAI), which was measured by the LAI-2200C instrument. Vegetation spectrum measurements can be divided into two parts. The first part was conducted in the Xinyuan pasture site and its surrounding areas from Aug. 27th to Sep. 12th, 2018, which was in coordinated with ground-based radiometer and radar observations. The main targets include the grassland and some other vegetation types, such as corn, carrot, potato and medicinal herbs etc. The second part was conducted over the selected quadrats in the Shandian river basin from Sep. 16th to Sep. 26th, 2018, which was coordinated with airborne remote sensing observations. The main vegetation types were grassland, along with carrot, buckwheat, potato and various vegetables.

In order to calibrate/validate airborne and satellite observations, one-month aerosol observations were conducted in the Shandian river basin from September to October 2018. Aerosol optical properties were measured using CE318 Sun photometer, which was installed in the Xinyuan pasture site. The automatic tracking Sun and sky scanning radiometers made direct Sun measurements with a 1.2° full field of view every 15 min at 340, 380, 440, 500, 675, 870, 940, and 1020 nm (nominal wavelengths). The direct Sun measurements take ~8 s to scan all 8 wavelengths (repeated three times within a minute), with a motor driven filter wheel positioning each filter in front of the detector. These solar extinction measurements are used to compute aerosol optical depth at each wavelength except for the 936 nm channel, which is used to retrieve total column water vapor (or precipitable water) in centimeters. Those observations of atmosphere properties were made concurrent with airborne missions and satellite overpasses, as atmospheric correction is a precondition for quantitative remote sensing.

3.4. Long-term ground observations

Not only to facilitate studies of water and energy exchanges at land-atmosphere at a regional scale, but also provide a long-term ground reference for validating various satellite products and the future TWRS, a soil moisture network needed to be established to represent the “ground truth” at a satellite pixel or model grid. In addition, soil temperature and precipitation are also critical variables needed for satellite products validation and assimilation. For this purpose, two networks were established for measuring those key variables, which are also essential for airborne experiments.

Installation of the network over the Shandian river basin started from Jul. 18th to Sep. 28th, 2018. The coverage of entire network is about 10,000 km^2 (115.5–116.5°E, 41.5–42.5°N), and the land surfaces are typically dominated by grasslands and croplands. There are three sampling scales including 100 km (large scale), 50 km (medium scale), and 10 km (small scale). These were initially designed to match the different scales of land surface modelling and various satellite retrievals (AMSR2, SMOS, SMAP and downscaled products). The layout of the large-scale soil moisture sites basically follows the M-shaped transect. The medium-scale sites are deployed as plum-shaped. The small-scale sites, which are exactly within a SMAP 9-km grid, are further nested and distributed as uniformly as possible according to realistic feasibility, as shown in Fig. 6.

The soil moisture sensors used were Decagon 5TM with 5 sensors (3, 5, 10, 20, and 50 cm depths) installed for each site. Of the 34 sites, 20 sites were equipped with a precipitation sensor. The data are recorded every 10 min. The power supply is provided by solar panels and all data can be transmitted wirelessly to a server. Undisturbed Soil samples at each layer of soil for each site were taken back to laboratory to analyze the gravimetric water content, bulk density and texture components for a further specific calibration.

Another network that consists of 30 sites in the Xiaoluan river basin was designed according to the AMSR2 grids with a spatial coverage of 25 km × 25 km. An intensive scale of 1 km is included inside for soil moisture downscaling. Unlike the Shandian river basin, the land surfaces in the Xiaoluan river basin are mainly forest and grassland (Fig. 6), with a relatively higher elevation varying from 1200 to 1800 m. Soil moisture and temperature are measured at only two soil depths (5 and 10 cm). The installation of this network took about two months from August to September 2018. Gravimetric water content and soil texture were also measured at each site to support further calibration.

The long-term measurement of evapotranspiration was conducted using the eddy covariance (EC) method over a cropland and grassland. From Aug. 15th to Sep. 5th, 2018, an EC system (CPEC200) was installed in a cropland (potato) with center pivot irrigation (115.95°E, 42.01°N). The whole system consists of a closed-path gas analyzer

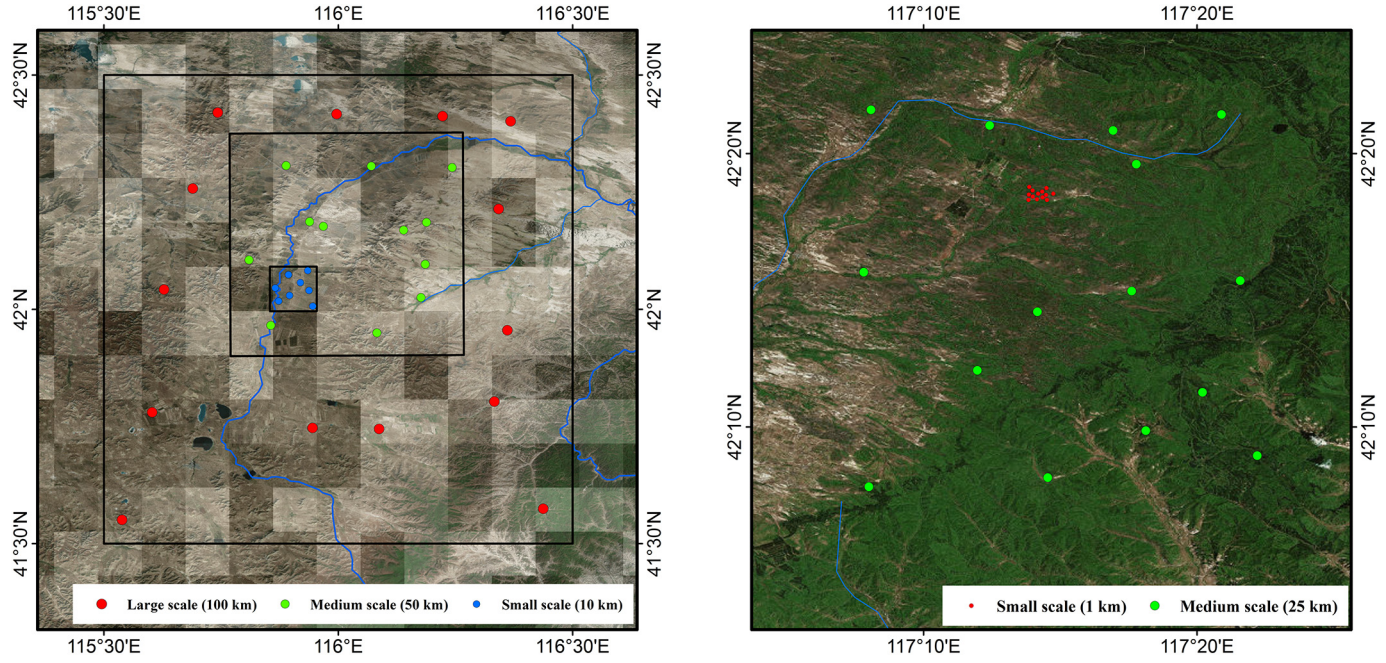

Fig. 6. The layout of soil moisture and temperature, precipitation network (Left: Shandian river basin with transparent gray grids indicating SMAP 9-km grids; Right: Xiaoluan river basin).

(EC155) to measure mixing ratios of CO_2 and H_2O, sonic anemometer (CSAT3A) to measure three-dimensional wind and sonic temperature, HMP155 humidity and temperature probe, CNR4 for measuring the energy balance, SI-111 infrared radiometer and a datalogger (CR3000). After Sep. 8th, 2018, the whole system was moved to the Xinyuan pasture site to continue the measurement.

The long-term observation system of surface radiation was installed in the Xinyuan pasture site in September. It was comprised of WS601 weather sensors for the measurement of temperature, relative humidity, precipitation, air pressure, wind direction and wind speed, four-component radiometer MR-60 to individually measure the short-wave radiation and the long-wave radiation in the upwards and downwards direction and a SI-111 infrared radiometer.

4. Methodologies

4.1. Microwave emission and scattering models

The simulation of microwave emission and scattering is normally performed using the zero-order solutions. For microwave emission from the land surface, the well-known tau-omega model (Mo et al., 1982) is presented as:

$$Tb_p^{total} = T_s(1 - R_p^s)\cdot e^{-\tau\bullet\sec\theta} + T_v(1-\omega)(1 - e^{-\tau\bullet\sec\theta})(1 + R_p^s\cdot e^{-\tau\bullet\sec\theta}) \quad (1)$$

where, the Tb_p^{total} is the brightness temperature at polarization of p, T_s and T_v are physical temperature of soil and vegetation, respectively. R_p^s is the polarized reflectivity of soil, which is a function of incidence angle θ, soil dielectric constant ϵ_r and soil surface roughness. τ and ω are vegetation optical depth and single scattering albedo to describe the absorbing and scattering effects of vegetation.

In this study, we use a parametric soil emission model (Zhao et al., 2015) to calculate the rough soil emissivity or reflectivity. This model is developed for accounting the L-band roughness effects under different incidence angels.

$$R_p^s = r_p\bullet A_p\bullet e^{(B_p\bullet m^2 + C_p\bullet m)} \quad (2)$$

where, $m = s^2/l$ is the geometric roughness parameter, and s, l are root mean squared height and correlation length, respectively. A_p, B_p *and* C_p are coefficients depending on the incidence angles. r_p is the specular reflectivity for the flat surface, and it is a function of incidence angle and soil dielectric constant, which is calculated by the Mironov model (Mironov et al., 2004).

For the microwave backscattering from the land surface, the water-cloud model (Attema and Ulaby, 1978) is used. The total backscatter is attributed to three main terms:

$$\sigma_{total}^0 = \sigma_s^0\bullet e^{-2\tau\bullet\sec\theta} + \sigma_{s+v}^0 + \sigma_v^0 \quad (3)$$

where, the first term represents the scattering form the soil layer with a two-way vegetation transmissivity. The second term represents the interaction between the vegetation canopy and the underneath soil, which is normally ignored. The third term is the scattering from the vegetation canopy that is given by (Eom and Fung, 1984):

$$\sigma_v^0 = 0.74\bullet\omega\bullet(1 + 0.54\bullet\omega\bullet\tau - 0.24\bullet\omega^2\bullet\tau^2)\bullet(1 - e^{-2.12\bullet\tau\bullet\sec\theta})\bullet\cos\theta \quad (4)$$

The backscatter coefficients of σ_s^0 are simulated by the advanced integral equation model (Chen et al., 2003) together with inputs of soil dielectric constants from the Mironov model (Mironov et al., 2004).

4.2. Soil moisture variability

Several researches have reported the soil moisture variability (Teuling and Troch, 2005; Famiglietti et al., 2008; Zarlenga et al., 2018), and Famiglietti et al. (2008) concluded that the relationship between the soil moisture standard deviation (σ) and mean moisture content (μ) can be expressed as an empirical function:

$$\sigma = k_1\bullet\mu\bullet e^{(-k_2\bullet\mu)} \quad (5)$$

where k_1 and k_2 are fitted parameters based on in situ measurements.

The soil moisture coefficient of variation (CV) as calculated by σ/μ can be represented from the Eq. (5) to an exponential function of μ:

$$CV = \frac{\sigma}{\mu} = k_1\bullet e^{(-k_2\bullet\mu)} \quad (6)$$

4.3. Diurnal temperature cycle

The diurnal temperature cycles are described by a harmonic-exponential model by Göttsche and Olesen (2001).

$$T_{day}(t) = T_{0,d} + T_a\bullet\cos[\pi\bullet\Omega^{-1}\bullet(t - t_m)],\ t \le t_s \quad (7)$$

$$T_{nig}(t) = T_{0,d+1} + [T_{day}(t_s) - T_1]\bullet e^{\frac{-(t-t_s)}{k}},\ t > t_s \quad (8)$$

where $T_{0,\,d}$ and $T_{0,\,d+1}$ are the minimum temperatures that change from day to day (Holmes et al., 2015), and T_a is the diurnal temperature amplitude. t_m and t_s are the time of maximum temperature and start of the cooling down process, respectively. Ω is the daytime length and k is the attenuation constant. This model describes the temperature during the most of daylight hours as a harmonic function. From time t_s to the next sunrise, it is modeled by an exponential decay function. Previous studies (Holmes et al., 2012; Holmes et al., 2015) indicate that the timing of maximum temperature could be expressed as: $t_m = t_n + \varphi + d\varphi$. Since t_n can be calculated from day of year and latitude, and timing offset φ is a fitted parameter, the phase shifts and amplitude changes for different soil depths could be parameterized as a function of vertical distance ($z_2 - z_1$) and damping depth z_D:

$$\mathrm{d}\varphi = \frac{z_2 - z_1}{z_D} \quad (9)$$

$$T_a^{z_2} = T_a^{z_1}\bullet e^{\frac{-\pi\bullet d\varphi}{24}} \quad (10)$$

where the damping depth z_D is an expression of the thermal diffusivity, which can be determined by soil moisture content and soil texture. Thus, there are only three parameters of T_0, T_a and φ that needs to be fitted on a day-to-day basis.

4.4. Soil moisture retrieval algorithm

The single channel algorithm (SCA), which is the baseline algorithm for the SMAP mission, was initially implemented to perform the soil moisture retrieval with airborne brightness temperature. The detailed description of SCA could be find in previous literatures (Jackson, 1993; O'Neill et al., 2018). In this algorithm, the soil surface emissivity of E_p^s is calculated by rearranging of Eq. (1):

$$E_p^s = 1 - R_p^s = \frac{E_p^{total} - 1 + e^{-2\tau\bullet\sec\theta} + \omega - \omega\bullet e^{-2\tau\bullet\sec\theta}}{e^{-2\tau\bullet\sec\theta} + \omega\bullet e^{-\tau\bullet\sec\theta} - \omega\bullet e^{-2\tau\bullet\sec\theta}} \quad (11)$$

The E_p^{total} can be obtained by assuming the vegetation temperature was equal to soil temperature. As the airborne observations lasted for more than 3 h, the soil temperature at time of data acquisition was obtained through the diurnal temperature cycle model, which was fitted pixel by pixel based on spatial interpolations from soil temperature network measurements at 3 cm. The vegetation correction was based on the land cover-driven vegetation parameters lookup table (b, ω and the stem factor) and normalized difference vegetation index (NDVI) derived vegetation water content, which was calculated from the Chinese GF-1 (Sep. 16th, 2018) and HJ-1B (Sep. 24th, 2018) data. The parametric soil emission model (Zhao et al., 2015) and the Mironov model (Mironov et al., 2004) were utilized to convert the soil surface emissivity to soil moisture with average values of soil roughness and texture from field measurements.

5. Preliminary results

5.1. Remote sensing data

5.1.1. Airborne observations

The L-band active-passive microwave sensor together with the optical imaging system were used to map the surface at various spatial resolution 4 times over the 70 km × 12 km region and 1 time over the 165 km × 5 km region. This simulated data at spatial resolutions consistent with future TWRS supports the testing of soil moisture retrieval and downscaling techniques based on multi-source satellite data. As noted above, the unique feature of the experiment is that the microwave observations would be taken at varying incidence angles. This is simulated by the special design with fine flight line spacing of 1 km, which is half of the coverage of airborne observations.

Fig. 7 presents the L-band radiometer and radar measurements on two different days (Sep. 24th and 26th) at selected incidence angles. Multi-angular radiometer observations were achieved by simply averaging the radiometer data within the range of target angle ± 1.25°, and multi-angular radar observations were accomplished by averaging the angular corrected radar data within the range of target angle ± 5°. For both radiometer and radar data, outliers above 3 standard deviations are removed within each grid (radiometer 1 km and radar 0.1 km), which is defined under the Equal-Area Scalable Earth (EASE) Grids 2.0. Conditions on Sep. 24th were relatively dry with an average soil moisture of 0.15 cm^3/cm^3 (all quadrats considered) after a dry-down following the rain event on Sep. 16th. In the central part of flight region, the brightness temperature is relatively low due to high soil moisture over wetlands. Relatively high values of brightness temperature were observed in the Northern part where grasslands dominate with an average soil moisture of 0.18 cm^3/cm^3 (quadrat 1–10). Rain events happened on Sep. 25th in the Northern part, and resulted in an increase of soil moisture to 0.26 cm^3/cm^3, which is reflected in a reduction of brightness temperature on Sep. 26th. However, the Southern part continued to dry down with an increase of brightness temperature. The radar data exhibits a similar pattern corresponding to the spatial-temporal variation of both soil moisture and vegetation. It also shows a reasonable angular dependence of the both radiometer and radar data.

Preliminary estimates of soil moisture were retrieved using radiometer-only observations based on the SCA algorithm at the vertical polarization (SCA-V). To apply the algorithm, the four days airborne data of brightness temperature were divided by the soil temperature obtained from the diurnal temperature cycle model (Eqs. (7) and (8)) to derive the total emissivity. The land cover classification from Gong et al., 2013 was resampled to 1-km resolution and used for setting vegetation related parameters according to SMAP look up table (O'Neill et al., 2018). The optical observations of NDVI from Chinese satellites (GF-1 and HJ-1B) were used to calculate the vegetation water content. Vegetation correction was then conducted by the Eq. (11) to obtain the soil surface emissivity, which was converted to soil moisture at individual incidence angles from 22.5° to 32.5°. The Fig. 8a shows the retrieved soil moisture from airborne data at incidence angle of 32.5°. It is shown that the northern area dominated by grasslands experienced a dry-down process from Sep. 17th to Sep. 24th, 2018, and the soil moisture values increased on Sep. 26th, 2018 due to the precipitation event on the day before. The southern area dominated by croplands experienced a continuous dry-down process during the 10 days from Sep. 17th to Sep 26th, 2018. Fig. 8b presents the average soil moisture estimated by the SMAP satellite from the baseline algorithm of SCA-V (SMAP_L3_SM_P_E, O'Neill et al., 2019), which shows a similar spatial-temporal variation pattern with airborne soil moisture estimates. The correlation coefficient between airborne and SMAP soil moisture is

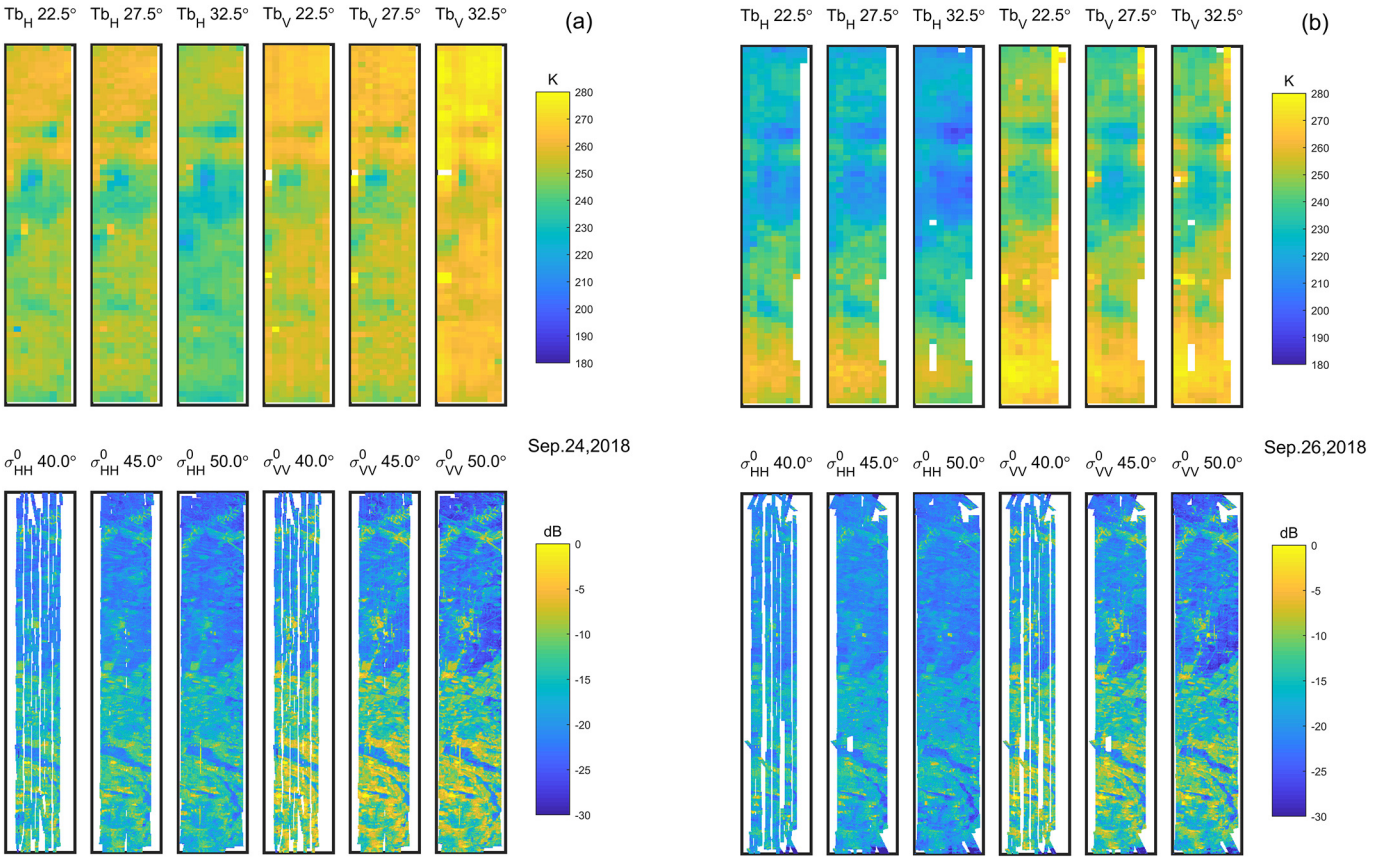

Fig. 7. Gridded multi-angle L-band radiometer (top, 1 km, 22.5°–32.5°, H and V polarization) and radar (bottom, 0.1 km, 40°–50°, HH and VV polarization) measurements for two days in the flight region #1 of 70 km × 12 km, representing dry (Sep. 24th, left, a) and wet (Sep. 26th, right, b) soil moisture conditions.

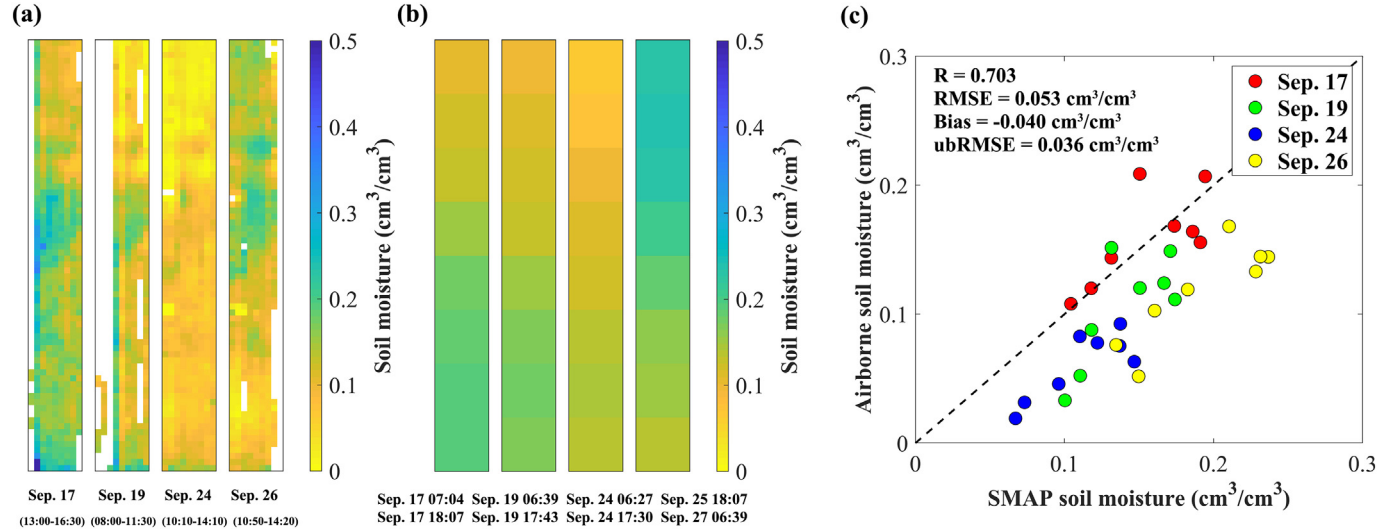

Fig. 8. Comparison of soil moisture estimates (SCA-V algorithm) from airborne and satellite observations. (a) Soil moisture retrieved from airborne brightness temperature, (b) soil moisture extracted from the SMAP_L3_SM_P_E product, (c) scatterplot of airborne and SMAP soil moisture.

0.703, and the root mean squared error (RMSE), bias and unbiased RMSE (ubRMSE) are 0.053 cm^3/cm^3, −0.04 cm^3/cm^3 and 0.036 cm^3/cm^3, respectively (Fig. 8c). The preliminary comparison demonstrates the reliability of airborne radiometer data, and a more detailed analysis of ground measurements, airborne and satellite observed soil moisture will be presented in a future study.

5.1.2. Ground-based observations

In addition to the airborne simulator, multi-angular observations of both active and passive microwave were also conducted at the ground scale. Fig. 9 shows the simultaneously observed brightness temperature (Fig. 9a) and backscatter coefficients (Fig. 9b) on Sep. 24th on the Xinyuan pasture site. The advanced integral equation model (Chen et al., 2003) and a parametric soil emission model (Zhao et al., 2015) were used to calculate the backscatter coefficient and emissivity from rough soil surface. As the grass is very short and its impacts on microwave signals are not significant, the zero-order solutions of water-cloud model (Attema and Ulaby, 1978) and tau-omega model (Mo et al., 1982) were used to account for vegetation effects. Those models (Eqs. (1) and (3)) with input measured parameters (soil moisture 0.129 cm^3/cm^3, soil temperature 287.35 K, root mean squared height 1.3 cm, correlation length 18 cm, and vegetation water content 0.5 kg/m^2; vegetation parameter b is set to be 0.13 and the scattering effect is ignored) are used to perform a preliminary simulation, which is found to generally match with the ground observations (performance statistics in Table 6). The RMSE between simulated and observed brightness temperature are 14.37 K and 13.56 K, respectively for horizontal and vertical polarizations. Ground-based observations of brightness temperature at lower incidence angles (< 35°) might be affected by the radiation of the truck, while observations at larger incidence angles (> 55°) might "see" emissions from the sky. The correlations between simulated and observed backscatter coefficients are quite high with

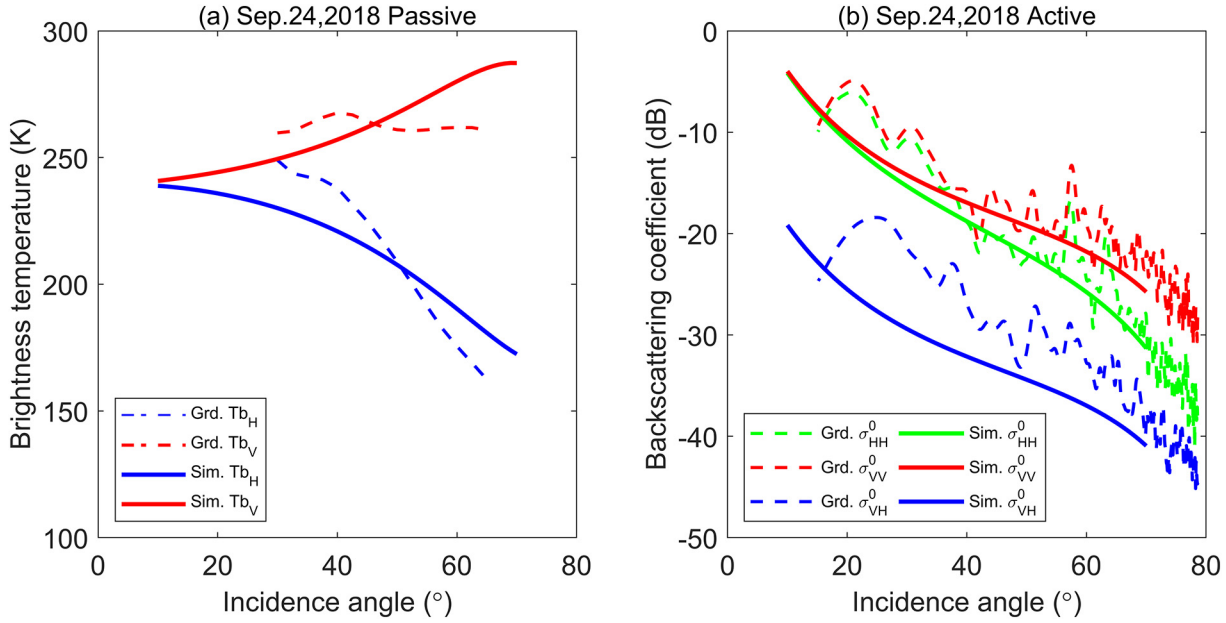

Fig. 9. Ground-based radiometer/radar observed and simulated L-band brightness temperature (a) and backscatter coefficient (b) over the Xinyuan pasture site on Sep. 24th (soil moisture = 0.129 cm^3/cm^3, soil temperature = 287.35 K, root mean squared height = 1.3 cm, correlation length = 18 cm, vegetation water content = 0.5 kg/m^2, vegetation parameter b = 0.13, single scattering albedo = 0).

Table 6
Statistics on the performance of L-band brightness temperature and backscatter coefficient simulations.

	R	RMSE	bias	ubRMSE
Sim. Tb_H vs. Grd. Tb_H	0.9970	14.3672 K	−2.7711 K	14.0975 K
Sim. Tb_V vs. Grd. Tb_V	−0.3126	13.5567 K	3.5997 K	13.0701 K
Sim. σ_{HH}^0 vs. Grd. σ_{HH}^0	0.9468	3.0065 dB	−1.9497 dB	2.2887 dB
Sim. σ_{VV}^0 vs. Grd. σ_{VV}^0	0.9192	3.1877 dB	−2.3513 dB	2.1524 dB
Sim. σ_{HV}^0 vs. Grd. σ_{HV}^0	0.8986	5.7786 dB	−5.1871 dB	2.5469 dB

correlation coefficients ranging from 0.90 (σ_{HV}^0) to 0.95 (σ_{HH}^0). The simulated backscatter coefficients generally show a negative bias, which is more significant at HV polarization with an ubRMSE < 2.6 dB. Those observations and their simulations further served as references for the airborne radiometer and radar calibration.

Fig. 10a and b present the relationships between L-band brightness temperature and backscatter coefficient at varying incidence angles over the pasture site. The data contain both dry (the cluster at the top left with soil moisture of 0.09 ± 0.02 cm^3/cm^3, before Aug. 26th) and wet (the cluster at the bottom right with soil moisture of 0.22 ± 0.03 cm^3/cm^3, after Aug. 28th) conditions, as caused by a rain event on Aug. 27th. Although the observed soil moisture ranged from 0.086 cm^3/cm^3 to 0.39 cm^3/cm^3 as shown in Fig. 10c, only a few microwave observations were obtained around the soil moisture value of 0.15 cm^3/cm^3. It was found that the active and passive observations are linearly correlated, which is the proposed theoretical basis for downscaling brightness temperature toward a higher spatial resolution for the SMAP mission (Das et al., 2011; Das et al., 2014). For the case of the TWRS, the incidence angles of active and passive observations vary but they both remain about equal with each other. Our preliminary analysis shows that the linear relationship exists not only for 40° but also for other incidence angles. As the incidence angles increase, the intercept of those linear relationships between Tb_H and σ_{HH}^0 gradually decreases (with the exception of 45°), while the slope only changes slightly. The correlation coefficients between Tb_H and σ_{HH}^0 reaches the strongest value of −0.95 at 30°, and generally better correlations are presented between Tb_V and σ_{VV}^0 with the strongest value of −0.95 at 35° as shown in Table 7. However, the hypothesis of the linear relationship between brightness temperature and backscatter needs further examination under varying incidence angle conditions, and those multi-angular airborne/ground-based remote sensing data will provide supports for the development of active-passive downscaling algorithm for the TWRS.

5.2. Ground measurements

5.2.1. Soil moisture

Volumetric soil moisture content (*SMC*) were measured with the 5TM and ML3 probes, which were both Frequency Domain

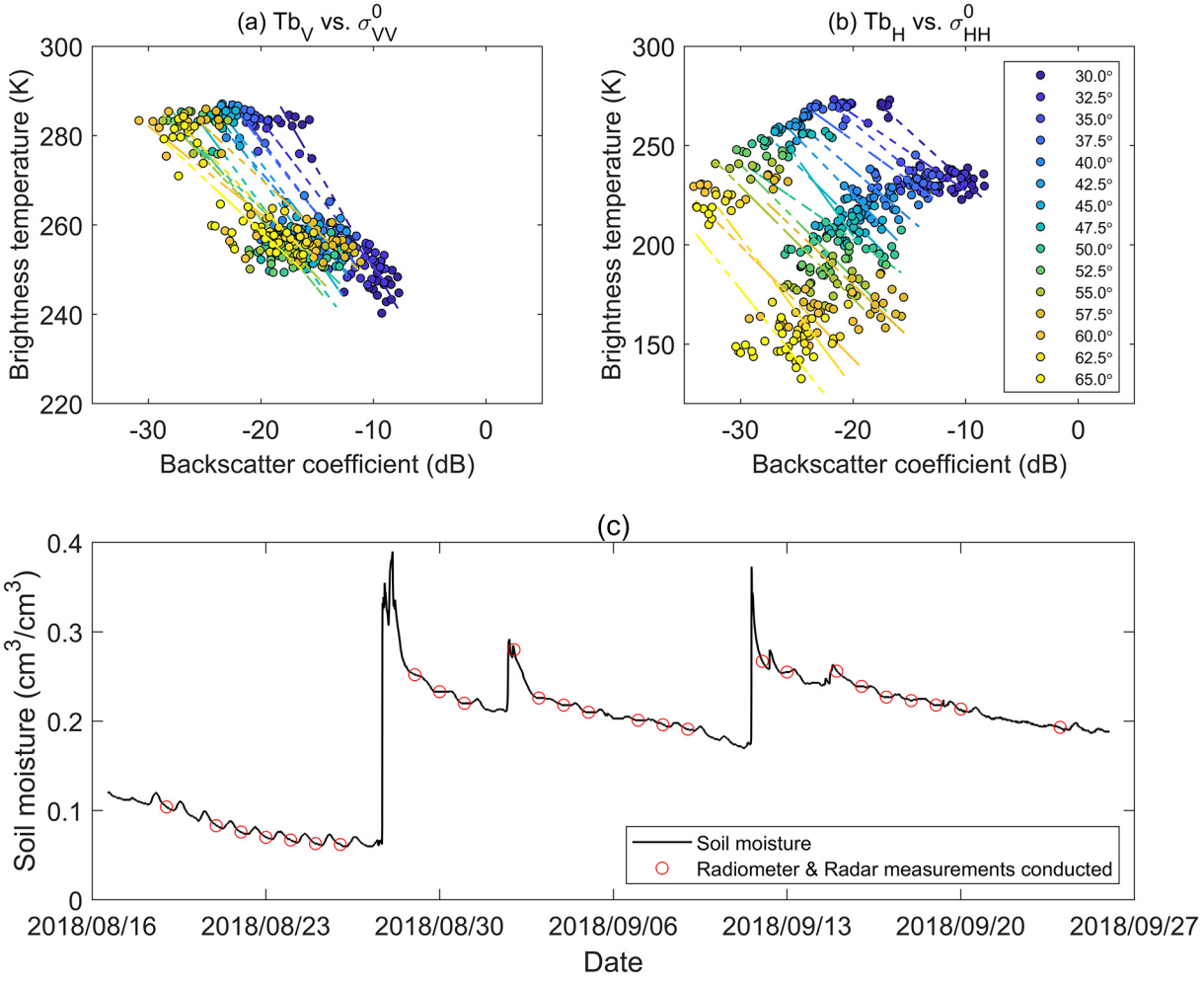

Fig. 10. Relationships between ground-based measurements of L-band brightness temperature and backscatter coefficient at varying incidence angles (a for Tb_V and σ_{VV}^0; b for Tb_H and σ_{HH}^0; dashed lines present the fitted linear relationships for different incidence angles). (c) is the observed soil moisture ranging from 0.086 cm^3/cm^3 to 0.39 cm^3/cm^3 with radiometer/radar measurement dates by red circles. (For interpretation of the references to color in this figure legend, the reader is referred to the web version of this article.)

Table 7
Slope, intercept and correlation coefficients of linear relationships between ground-based measurements of L-band brightness temperature and backscatter coefficient at selected incidence angles.

	Tb_V and σ_{VV}^0			Tb_H and σ_{HH}^0		
Incidence angle	Slope	Intercept	Correlation	Slope	Intercept	Correlation
30°	−4.3380	207.3029	−0.9447	−5.1712	179.5696	−0.9487
35°	−3.3401	212.3298	−0.9463	−4.7489	166.5050	−0.9241
40°	−2.9160	213.5123	−0.8776	−4.8771	140.0762	−0.8811
45°	−3.6675	197.4040	−0.9240	−5.6935	97.9991	−0.8510
50°	−2.3968	215.7393	−0.9083	−3.8998	124.6626	−0.7206
55°	−2.6426	208.7442	−0.8552	−5.6505	59.8634	−0.8111
60°	−1.9692	223.0549	−0.8886	−5.7036	28.3511	−0.8352
65°	−2.3536	211.4348	−0.8877	−7.0607	−34.4143	−0.7977

Reflectometry (FDR) type sensors. Measurements by FDR sensors were preliminarily calibrated by using soil samples results from the oven drying (thermogravimetric) method. The number of soil samples associated with the 5TM sensor at fixed soil moisture and temperature sites is 170 (5 depths for 34 sites). The sand, silt and clay of those collected samples ranges 29.3%~94.5%, 2%~55.9%, 1.6%~24.4% respectively and these soils were mainly categorized as sandy loam. During the ground sampling campaign, 168 samples were taken for the ML3 sensor. The comparison shown in Fig. 11 suggests a strong correlation between FDR measurements and thermogravimetric values. The correlation coefficients for the 5TM and ML3 sensors are 0.824 and 0.834, respectively. The raw values of the 5TM sensor tend to underestimate the soil moisture with a bias of 0.026 cm^3/cm^3 and ubRMSE of 0.065 cm^3/cm^3, while the ML3 sensor tend to overestimate the soil moisture with a lower ubRMSE of 0.054 cm^3/cm^3. Preliminary calibration functions for both sensors are:

$$SMC_v = 1.0614 \bullet SMC_{5TM} + 0.0134 \quad (12)$$

$$SMC_v = 0.8391 \bullet SMC_{ML3} + 0.0280 \quad (13)$$

The spatial pattern of soil moisture measured from both the network and campaign are plotted in Fig. 12 for the flight region #1 (70 km × 12 km). The soil moisture over this region ranged from ~0.1 to ~0.5 cm^3/cm^3, with higher soil moisture values in the north central area dominated by grassland and wetland, and lower soil moisture values in the southern area dominated by cropland. As crops were close to the time of maturity and harvest, soils were dry due to no further irrigation control. From Sep. 15th, 2018, the soil moisture was generally undergoing a drying down process. Precipitation occurred on Sep. 25th, 2018 around the Zhenglan Banner, and most of quadrats in the northern area wetted up while the soil in the southern area continued to dry. Therefore, in general, this experiment covers a wide range of soil moisture condition.

The spatial variability of soil moisture is affected by many controlling factors including the hydraulic properties of the soil, topography, precipitation and vegetation cover etc. The understanding of the spatial variability of soil moisture is important for uncertainty estimation of hydrological models, the upscaling issue when setting up a measurement network, and downscaling issue for validation of remote sensing products. Soil moisture variability across scales are studied by exploring the coefficient of variation (Eq. (6)) and standard deviation as a function of the mean soil moisture values (Eq. (5)) for each 200-m quadrat (Fig. 13). As each location was measured for 3–6 times, only quadrats with measurements > 18 times are taken into calculation. Results show that the relative variation in soil moisture generally decreases as the soil moisture increase. For the 200-m scale in our measurement, the relationship between soil moisture standard deviation versus mean soil moisture present to be an upward concave shape with the maximum value of ~0.1 cm^3/cm^3 at around 0.35 cm^3/cm^3. It is argued that this relationship could be related to the spatial variability in soil hydraulic properties (Vereecken et al., 2008). But results show widely scattered values around the fitted empirical functions, especially when soil is dry. It is indicated that the spatial variability over our experimental area is complex and should be affected by many other factors that needs further studies. Those manually sampled data together with data from the built network should serve as a fundamental basis for the scaling study of soil moisture.

5.2.2. Ground temperatures

Ground temperatures including soil effective temperature and vegetation temperature are essential parameters for accurate soil moisture retrieval. For the SMOS/SMAP missions that only carry an L-band instrument, they must rely on the inputs from numerical weather prediction models for temperature. For the TWRS, infrared observations would be available to provide temperature information under clear skies. These measurements would be for only the shallowest depth of the land surface but with higher spatial resolution. It is possible to separate the vegetation temperature and soil temperature, which could be used to estimate the effective soil temperature by accounting for the damping effects. To examine the temperature difference of soil and vegetation, we take temperature measurements collected by the thermistor of TR-52i, as shown in Fig. 14. It is shown that the vegetation temperature is generally lower than the soil temperature with a bias of −1.62 K. The soil and vegetation temperature are equal or closer at the morning time, at which the land surface conditions are expected to be closest to thermal equilibrium. As the vegetation in this area is relatively short and sparse, the soil temperature is higher than vegetation temperature in the afternoon. The difference between soil and vegetation temperature reaches its maximum of about 11 K at around solar noon. This further indicates that the separate information of soil and

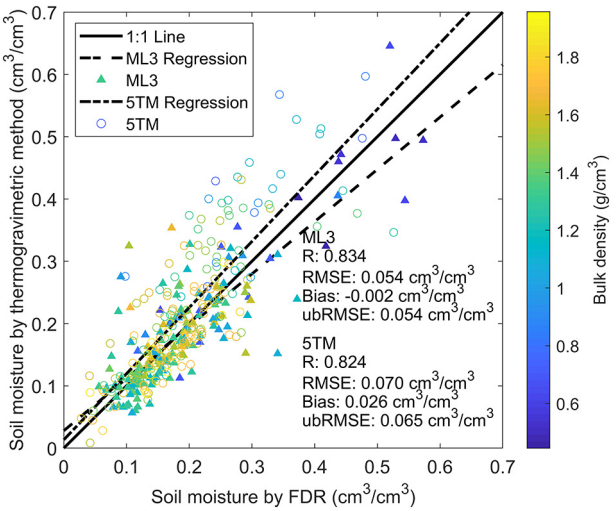

Fig. 11. Comparison of thermogravimetric and FDR soil moisture measurements (5TM: hollow circle; ML3: solid triangle) for varying bulk density.

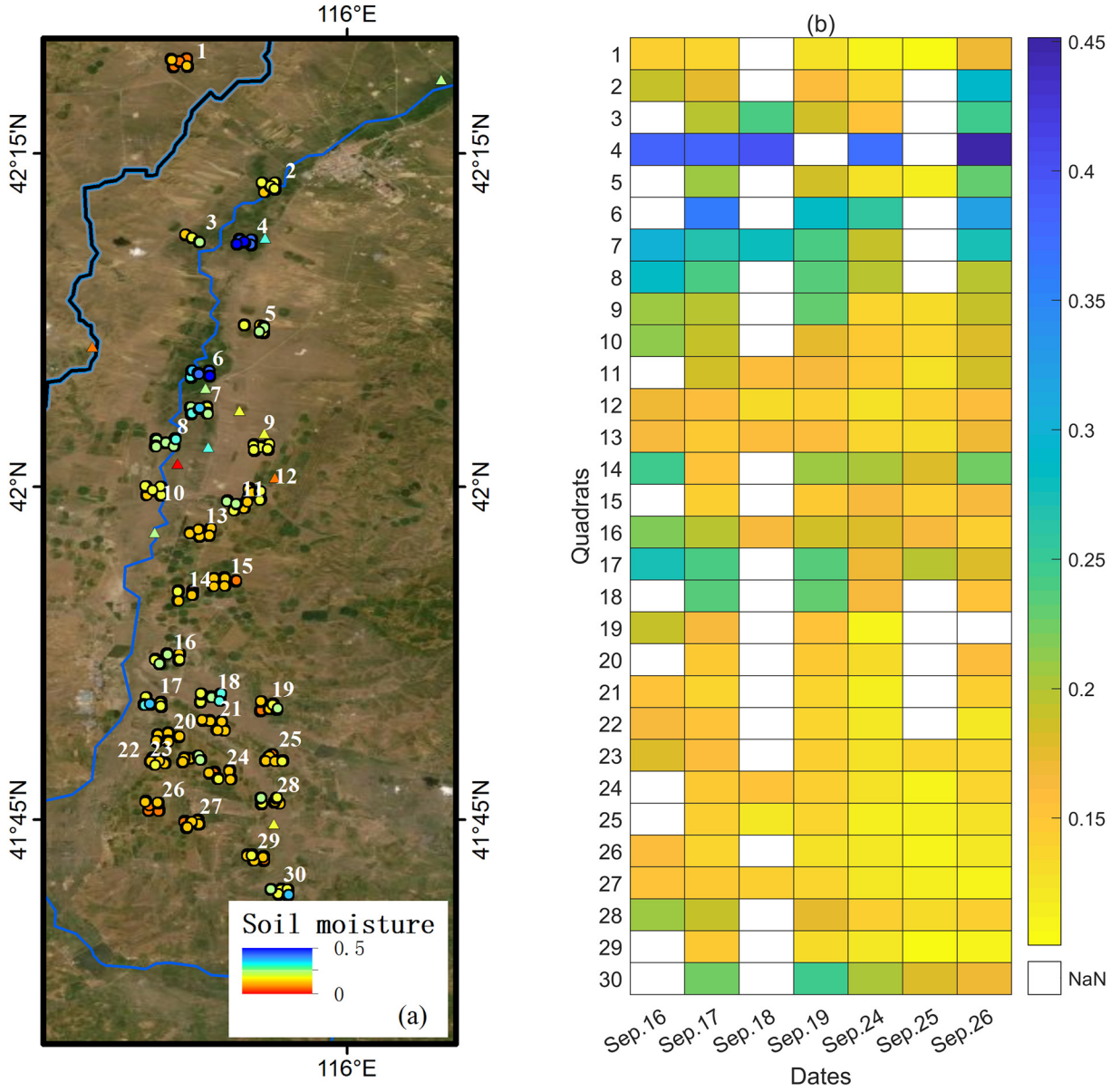

Fig. 12. Spatial pattern (a, Sep. 17th, 2018, circled points indicating sample results from the ground campaign and triangle points are from fixed sites) of 5-cm soil moisture and its temporal evolution (b) over large quadrats, which were numbered from 1 to 30 in order from north to south.

vegetation information is important for soil moisture mission operating with local overpass time in the afternoon.

In addition, soil temperature measurements at four different depths (3, 5, 10 and 20 cm) from the network are averaged for all available sites and the whole experimental period (16th Sep to 30th Sep), as colored dots shown in Fig. 15. The solid color lines are fitted diurnal temperature cycles for different soil depth according to Eqs. (7) and (8). It is shown that the soil temperatures within top 10 cm are closest to each other at around 10 A.M. and 19 P.M. in the experimental area. The timing of the maximum soil temperature at 3 cm is 3.63 h after solar noon, and the timing for other soil depths are further delayed until the latest one of 20.96 P.M. at 20 cm. The phase shift is 0.18 h over 3 cm vertical distance and increases to 1.17 h due to the large vertical distance of 20 cm. The temperature amplitude of the harmonic is reduced as the soil depth increases. This fitting could be accomplished on a day-to-day basis for each site, in support of obtaining soil temperature information at any time. In addition, it also implies that, through phase synchronization and amplitude adjustment, the surface temperature by thermal infrared observations could be transferred to soil temperature and then to effective soil temperature, which is required for accurate soil moisture retrievals with airborne data and future satellite observations.

5.2.3. *Vegetation water content*

Vegetation water content was measured in August and September 2018. There were approximately 100 vegetation samples collected, including 45 samples prior to the airborne experiment and 55 samples during the airborne campaign. As shown in Fig. 16(a), vegetation types include grass, potato, carrot, millet, buckwheat, corn, astragalus and radix isatidis. The corn plants contained the largest water content varying with density and growth stage. The grass water content also depended on the density and height, but varied little through the campaign, with generally the smallest values (< 0.5 kg/m^2). The water content of buckwheat and carrot were about 1 kg/m^2 and 2.8 kg/m^2 respectively during the campaign. The vegetation water content of millet and potato varied significantly due to differences in planting densities, seeding dates, and management conditions. Around Sep. 25th, the latter half of the campaign, crops began to be harvested. Thus,

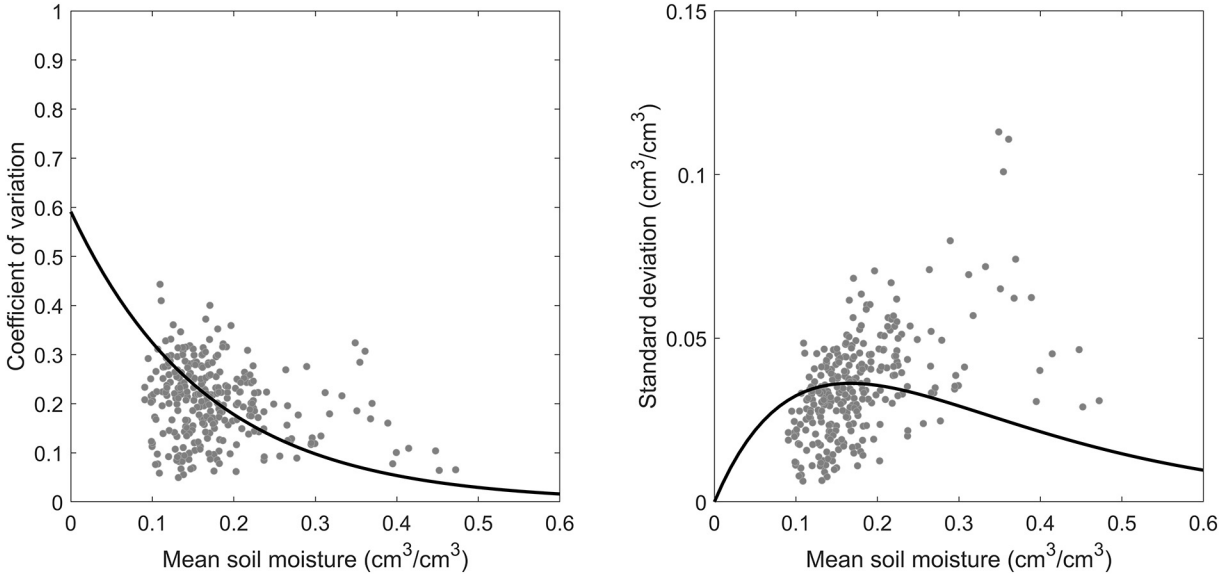

Fig. 13. Coefficient of variation and standard deviation versus mean soil moisture content measured at the 200-m scale quadrats during the ground sampling campaign, including the 70 km × 12 km flight region (Sep. 16th, Sep. 17th, Sep. 18th, Sep. 19th, Sep. 24th, Sep. 25th, and Sep. 26th) and the 165 km × 5 km flight region (Sep. 20th). Solid lines are fitted relationships according to Eqs. (5) and (6).

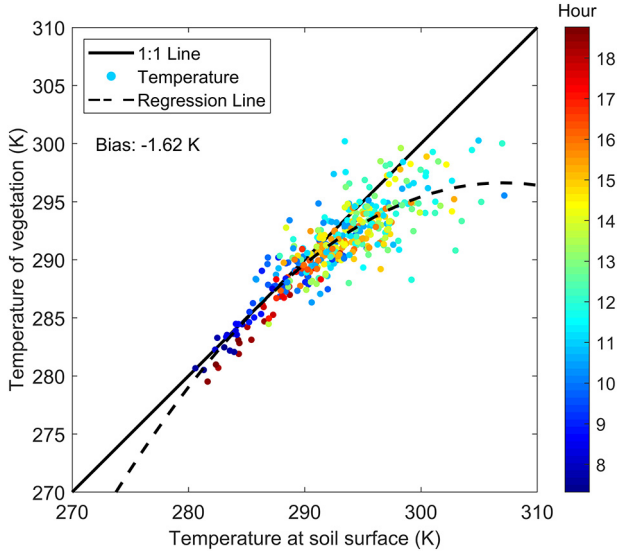

Fig. 14. Comparison of soil surface and vegetation (grass and crops) temperatures measured during the ground sampling campaign, including the 70 km × 12 km flight region (Sep. 16th, Sep. 17th, Sep. 18th, Sep. 19th, Sep. 24th, Sep. 25th, and Sep. 26th) and the 165 km × 5 km flight region (Sep. 20th). The dashed curve is the fitted relationship between vegetation temperature and soil temperature.

the vegetation conditions can change significantly especially in the southern area with cropland dominated. As mentioned above, the vegetation spectrum and LAI were also measured at the ground for selected sampling fields. Fig. 16(b) shows the relationships of vegetation water content with matched ground-measured NDVI and LAI, which are used for SMAP and SMOS missions respectively as a complementary vegetation information. NDVI and LAI measurements were conducted at the stage when vegetation approached maturity. It is shown that NDVI has a high sensitivity to vegetation water content when it is < 1 kg/m^2, but its sensitivity decreases significantly and starts to saturate as vegetation water content is > 1 kg/m^2. The LAI of crops and grass was found to be linearly correlated to vegetation water content, which is consistent with the adoption in the SMOS soil moisture algorithm (Wigneron et al., 2004; Kerr et al., 2012). Further studies would be carried out on how to use optical observations to efficiently provide complementary information on vegetation properties (vegetation coverage, water content and optical depth etc.) for soil moisture retrieval from the TWRS.

5.3. Sensitivity analysis

A first step to evaluate the remote sensing data is to assess its sensitivity to surface soil moisture. All the multi-angular passive and active microwave remote sensing data obtained during the airborne experiment are used to compare the correlations. The sensitivity of microwave brightness temperature to soil moisture was examined as shown in Fig. 17. The soil moisture is the mean value within the 1 km × 2 km quadrat, and the brightness temperature is the averaged value of all footprints (± 1.25°) within each quadrat. The sensitivity at different incidence angles and polarizations are similar with brightness temperature decreasing as soil moisture increases, due to the decrease in emissivity of wet soils. It shows a "triangle" correlation obtained between brightness temperature and surface soil moisture as expected based on previous studies (Merlin et al., 2008; Panciera et al., 2014; McNairn et al., 2015). The correlation coefficients between V polarized brightness temperature and soil moisture are −0.49, −0.60, −0.62, −0.64, and −0.62 for different incidence angles (22.5° to 32.5°). The correlation is enhanced at H polarization in the value of −0.68, −0.68, −0.69, −0.61 and −0.71, respectively. And the slope of relationship is also higher for H polarization than at V polarization, indicating higher sensitivity to soil moisture at H polarization. It is also indicated that the passive microwave observations can have stronger correlation and higher sensitivity with soil moisture at larger incidence angles within the range from 22.5° to 32.5°. In addition, these results demonstrate that SMELR captured a very large range of response for both brightness temperature (~80 K) and soil moisture (0.1–0.5 cm^3/cm^3), which is rare in an aircraft-based field experiment.

Fig. 18 further explores the sensitivity of radar backscatter coefficient to soil moisture at different incidence angles within the 200 m × 200 m quadrat. The backscatter coefficient is the averaged value (± 2.5°) within each quadrat. It is found the backscatter coefficient exhibits a generally positive correlation with soil moisture. The sensitivity is more significant for grasslands with the highest correlation

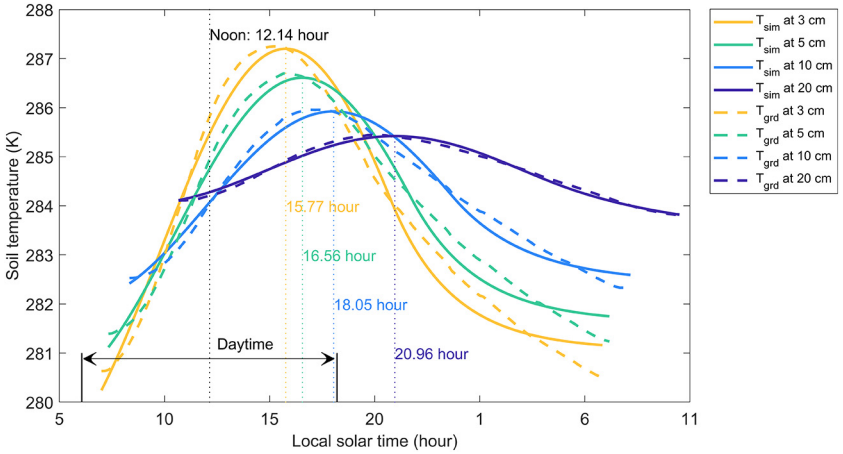

Fig. 15. The observed (T_{grd}) and modeled (T_{sim}) diurnal soil temperature cycles at different soil depth from the soil moisture and temperature network. Colored dashed and solid lines are averaged in situ measurements and fitted models, respectively. Colored dots illustrate the timing delayed (amplitude damping) from the solar noon time (black dots).

coefficient of 0.64 and 0.52 for VV and HH polarization, respectively. This is because the vegetation and surface roughness over the grassland do not vary a lot, and the soil moisture is the main contribution to the variation of backscatter coefficient. However, there is a large scatter in the comparison between backscatter coefficient and soil moisture over croplands. This is likely due to the effects of vegetation structure and water content of different crop types and surface roughness, which have a large dynamic change. During the ground sampling of soil moisture, there are ten different crop types including potatoes, carrots, wheat, corn, cabbage etc. There can be significant difference in terms of scatter shape and size, which makes the backscattering quite complex. For example, even for the same field of potatoes with ridging, the backscatter coefficient with the similar incidence angles can be different as the azimuth angle is different from opposite flights. This indicates that it is more challenging to retrieve accurate soil moisture from radar observations, and on the other hand, the radar observations can provide complementary information to radiometer for better vegetation and roughness correction. It should be noted that both the active and passive remote sensing data and ground measured soil moisture contains uncertainty that needs to be examined in subsequent use and studies. The synergy between active and passive microwave observations and their relationship with soil moisture show expected variation to soil moisture changes, vegetation and roughness factors, which can be exploited for development of soil moisture retrieval algorithms and downscaling techniques from observations of TWRS, which is beyond the scope of experiment overview presented here.

6. Summary and conclusions

SMELR was the first active-passive microwave and optical synergistic observation airborne experiment conducted in China. Its purpose was to support a proposed Chinese TWRS. This satellite will use combined L-band active and passive microwave instrument as the main tool to map global soil moisture at high-resolution (~1 km, radar-based), low-resolution (~20 km, radiometer-based), and intermediate-resolution (~5 km, combined active-passive). A major different from previous SMOS and SMAP mission, is that this satellite will also carry optical sensors including thermal infrared, multispectral and hyperspectral cameras to provide auxiliary information. This will provide new opportunities to improve the accuracy and spatial resolution of soil moisture mapping but also bring new issues. The SMELR experiment was designed to provide an airborne data set for algorithm development and testing for this mission. It is pivotal for the terrestrial water resource mission demonstration and is also urgent for insuring continuity of L-band observations from space.

Airborne observations and supporting ground data were collected over the upper stream of the Luan River basin for potential hydrologic applications. The experimental domain covers an area of 2° × 2° with

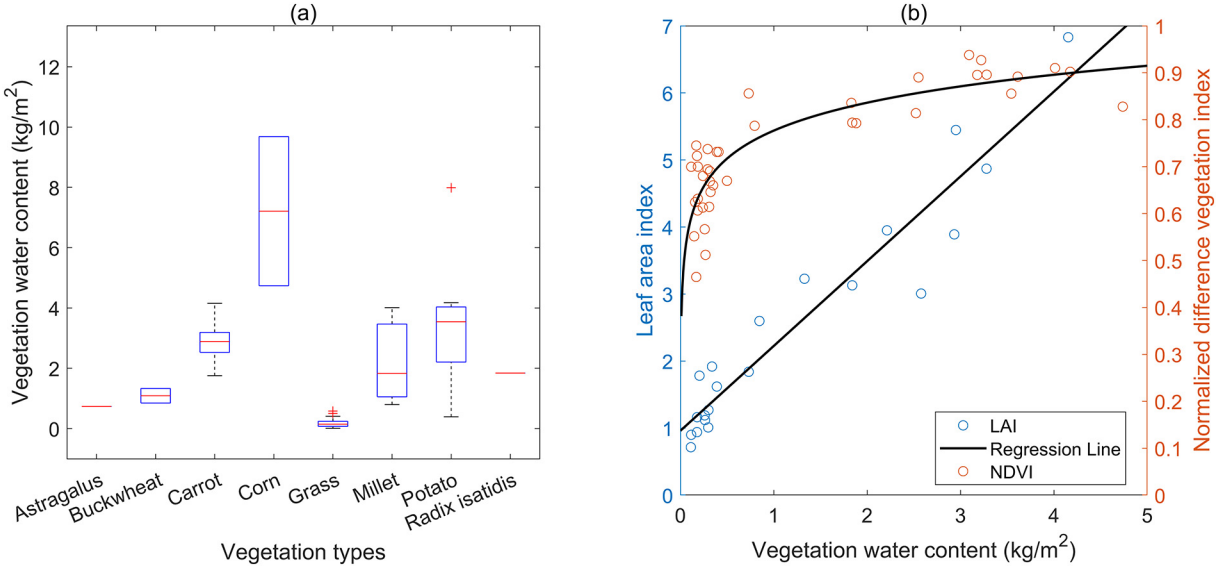

Fig. 16. The boxplot of vegetation water content for various vegetation types (a) and its relationships with ground-measured NDVI and LAI (b). Measurements of vegetation were gathered prior to and during the airborne campaign. Solid lines are fitted relationships between vegetation water content and NDVI/LAI.

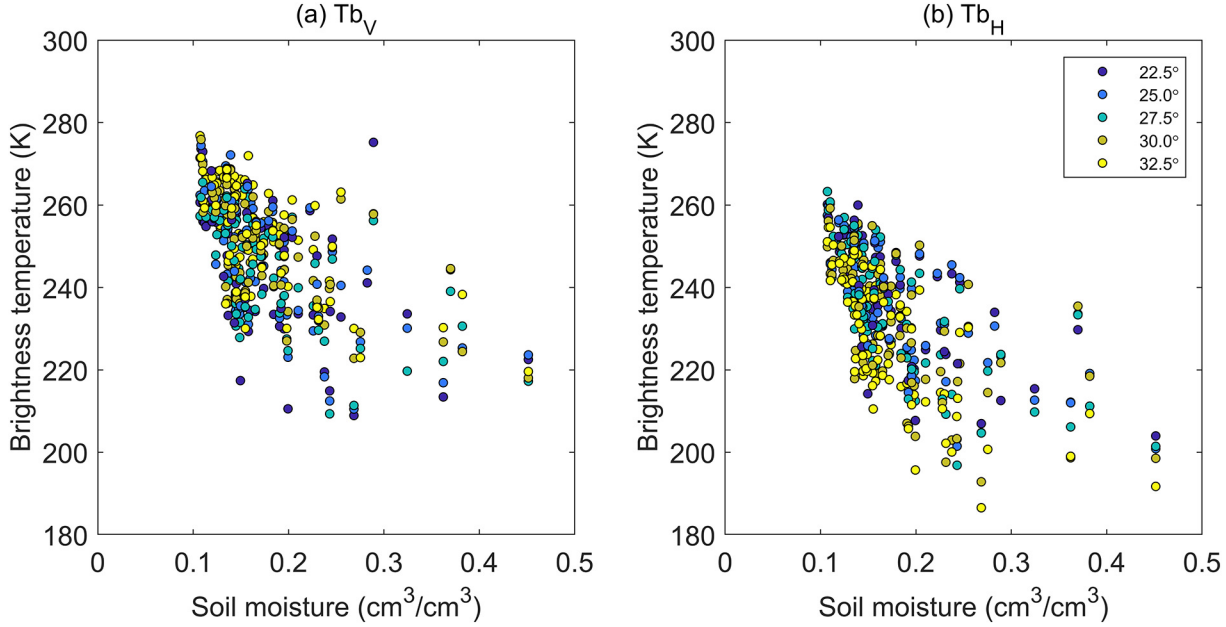

Fig. 17. Airborne observed radiometer brightness temperature versus ground measured soil moisture (0–5 cm) within 1 km × 2 km quadrats in the flight region #1 of 70 km × 12 km.

various land covers including grassland, croplands, forest, shrublands and bare ground. 5 flights were conducted, and multi-angular observations of both active and passive microwave together with infrared, multispectral and hyperspectral data were obtained to explore the impacts of scaling issues, as well as the incidence angle effects associated with the 1-D synthetic aperture technology. Concurrent ground data collection included soil moisture, ground temperature, vegetation water content and surface roughness. The soil moisture was sampled at different resolutions including the 1 km × 2 km quadrat (radiometer resolution) and 200 m × 200 m quadrat (radar resolution). In addition, two soil moisture and temperature networks were established in the Shandian River and Xiaoluan River basin, toward future soil moisture products validation. It was found that both the 5TM and ML3 FDR sensors could provide reliable measurements of soil moisture with correlation coefficients of 0.824 and 0.834 compared to thermogravimetric values.

SMELR resulted in the observation of a wide range of land surface conditions including almost the full range of soil moisture (0.1–0.5 cm^3/cm^3) and vegetation water content up to 7 kg/m^2. Correspondingly, the L-band active and passive observations exhibited a very large variation of ~30 dB and ~80 K, respectively. The soil moisture presents different uncertainty at different spatial scales, and the standard deviation was maximum at the intermediate soil moisture value of around 0.35 cm^3/cm^3. The soil and vegetation temperature difference were found to be maximum around noon time, and the soil temperature gradient was largest around 15.0 P.M. in the experimental

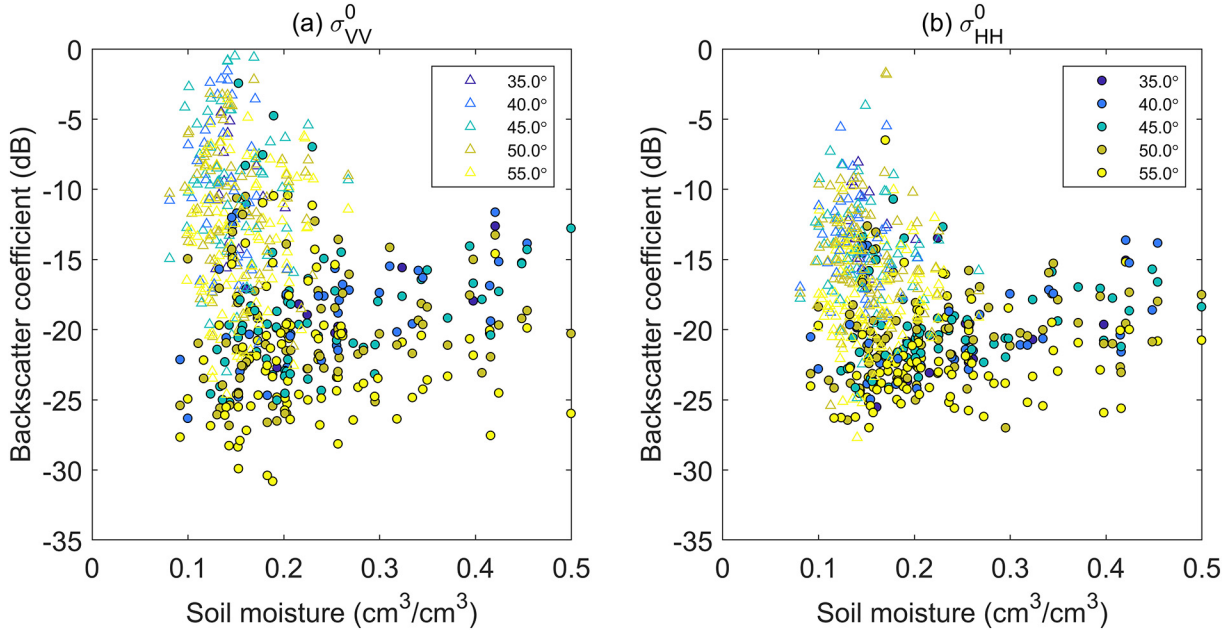

Fig. 18. Airborne observed radar backscatter coefficient versus ground measured soil moisture (0–5 cm) within 200 m × 200 m quadrats in the flight region #1 of 70 km × 12 km. Colored dots represent the grassland, and colored triangles represent the cropland.

area. This needs to be taken into account because the TWRS will operate in an afternoon orbit. The multi-angular infrared camera onboard is targeted to provide detailed surface component temperatures. The observed NDVI and LAI show good correlation with vegetation water content, and its synergistic use with radar observations would strengthen the ability for better vegetation correction. Preliminary analysis shows good sensitivity of active and passive microwave data to soil moisture. The radar data are not only sensitive to soil moisture but also to changing vegetation properties and surface roughness. This provides a unique data set to explore the synergy of active, passive microwave and optical data for soil moisture mapping at improved accuracy and resolution. The experiment overview and preliminary analysis of remote sensing and ground data have confirmed the SMELR data set will help to address a variety of prelaunch science questions of terrestrial water resource mission, including implementation of observing system simulation experiments at regional scales for identifying the mission requirements, development of robust retrieval algorithms and downscaling methods under varying incidence angles, exploration of multi-source data fusion solutions for improving the soil moisture accuracy and resolution, examination methodologies for calibration and validation of data products etc., which are out of the current scope of this paper and will be presented in future studies.

The data described in this paper is available from the web site at www.slrss.cn, which provides all the airborne and ground data together with documents for interpretation. Data can be accessed after signing the data usage agreement, and acknowledgement in any publication arising from the use of these data is required.

Author contribution statement

Tianjie Zhao: Conceptualization, Methodology, Formal analysis, Investigation, Writing - Original Draft
Jiancheng Shi: Supervision, Funding acquisition
Liqing Lv: Project administration
Hongxin Xu: Resources
Deqing Chen: Resources
Qian Cui: Methodology, Data Curation
Thomas J. Jackson: Formal analysis, Writing - Review & Editing
Guangjian Yan: Investigation
Li Jia: Investigation
Liangfu Chen: Investigation
Kai Zhao: Investigation
Xingming Zheng: Data Curation
Limin Zhao: Data Curation
Chaolei Zheng: Data Curation
Dabin Ji: Data Curation
Chuan Xiong: Data Curation
Tianxing Wang: Data Curation
Rui Li: Data Curation
Jinmei Pan: Data Curation
Jianguang Wen: Data Curation
Chao Yu: Data Curation
Yaomin Zheng: Data Curation
Lingmei Jiang: Data Curation
Linna Chai: Data Curation
Hui Lu: Data Curation
Panpan Yao: Data Curation
Jianwei Ma: Data Curation
Haishen Lv: Data Curation
Jianjun Wu: Data Curation
Wei Zhao: Data Curation
Na Yang: Data Curation
Peng Guo: Data Curation
Yuxia Li: Data Curation
Lu Hu: Data Curation
Deyuan Geng: Data Curation
Ziqian Zhang: Data Curation

Acknowledgments

This study was supported by the National Basic Research Program of China (2015CB953701, National Key Research and Development Program of China (2016YFE0117300), the 13th Five-Year Plan of Civil Aerospace Technology Advanced Research Projects (Y7D0070038), National Natural Science Foundation of China (41671355) and Youth Innovation Promotion Association (2016061). The authors would like to thank hundreds of scientists, engineers, and students who participated in SMELR field campaigns to make the experiment a great success.

References

Al-Yaari, A., Wigneron, J.-P., Dorigo, W., Colliander, A., Pellarin, T., Hahn, S., Mialon, A., Richaume, P., Fernandez-Moran, R., Fan, L., Kerr, Y.H., De Lannoy, G., 2019. Assessment and inter-comparison of recently developed/reprocessed microwave satellite soil moisture products using ISMN ground-based measurements. Remote Sens. Environ. 224, 289–303. https://doi.org/10.1016/j.rse.2019.02.008.

Attema, E.P.W., Ulaby, F.T., 1978. Vegetation modeled as a water cloud. Radio Sci. 13, 357–364.

Bindlish, R., Jackson, T.J., Gasiewski, A.J., Klein, M., Njoku, E.G., 2006. Soil moisture mapping and AMSR-E validation using the PSR in SMEX02. Remote Sens. Environ. 103, 127–139. https://doi.org/10.1016/j.rse.2005.02.003.

Bindlish, R., Jackson, T.J., Gasiewski, A., Stankov, B., Klein, M., Cosh, M.H., Mladenova, I., Watts, C., Vivoni, E., Lakshmi, V., Bolten, J., Keefer, T., 2008. Aircraft based soil moisture retrievals under mixed vegetation and topographic conditions. Remote Sens. Environ. 112, 375–390. https://doi.org/10.1016/j.rse.2007.01.024.

Bindlish, R., Jackson, T., Sun, R., Cosh, M., Yueh, S., Dinardo, S., 2009. Combined passive and active microwave observations of soil moisture during CLASIC. IEEE Geosci. Remote Sens. Lett. 6, 644–648. https://doi.org/10.1109/LGRS.2009.2028441.

Bogena, H.R., Huisman, J.A., Schilling, B., Weuthen, A., Vereecken, H., 2017. Effective calibration of low-cost soil water content sensors. Sensors 17, 208. https://doi.org/10.3390/s17010208.

Bonan, G.B., Stillwell-soller, L.M., 1998. Soil water and the persistence of floods and droughts in the Mississippi river basin. Water Resour. Res. 34, 2693–2701.

Brocca, L., Ciabatta, L., Massari, C., Camici, S., Tarpanelli, A., 2017. Soil moisture for hydrological applications: open questions and new opportunities. Water 9, 140. https://doi.org/10.3390/w9020140.

Chan, S.K., Bindlish, R., Neill, P.O., Jackson, T., Njoku, E., Dunbar, S., Chaubell, J., Piepmeier, J., Yueh, S., Entekhabi, D., Colliander, A., Chen, F., Cosh, M.H., Caldwell, T., Walker, J., Berg, A., Mcnairn, H., Thibeault, M., Martínez-fernández, J., Uldall, F., Seyfried, M., Bosch, D., Starks, P., Holi, C., Prueger, J., Van Der Velde, R., Asanuma, J., Palecki, M., Small, E.E., Zreda, M., Calvet, J., Crow, W.T., Kerr, Y., 2018. Development and assessment of the SMAP enhanced passive soil moisture product. Remote Sens. Environ. 204, 931–941. https://doi.org/10.1016/j.rse.2017.08.025.

Chen, K.S., Wu, T.D., Tsang, L., Li, Q., Shi, J., Fung, A.K., 2003. Emission of rough surfaces calculated by the integral equation method with comparison to three-dimensional moment method simulations. IEEE Trans. Geosci. Remote Sens. 41, 90–101. https://doi.org/10.1109/TGRS.2002.807587.

Colliander, A., Cosh, M.H., Misra, S., Jackson, T.J., Crow, W.T., Chan, S., Bindlish, R., Chae, C., Holi, C., Yueh, S.H., 2017. Validation and scaling of soil moisture in a semi-arid environment: SMAP validation experiment 2015 (SMAPVEX15). Remote Sens. Environ. 196, 101–112. https://doi.org/10.1016/j.rse.2017.04.022.

Corradini, C., 2014. Soil moisture in the development of hydrological processes and its determination at different spatial scales. J. Hydrol. 516, 1–5. https://doi.org/10.1016/j.jhydrol.2014.02.051.

Cosh, M.H., Jackson, T.J., Starks, P., Heathman, G., 2006. Temporal stability of surface soil moisture in the Little Washita River watershed and its applications in satellite soil moisture product validation. Remote Sens. Environ. 323, 168–177. https://doi.org/10.1016/j.jhydrol.2005.08.020.

Cosh, M.H., Kabela, E.D., Hornbuckle, B., Gleason, M.L., Jackson, T.J., Prueger, J.H., 2009. Observations of dew amount using in situ and satellite measurements in an agricultural landscape. Agric. For. Meteorol. 149, 1082–1086. https://doi.org/10.1016/j.agrformet.2009.01.004.

Das, N.N., Entekhabi, D., Member, S., Njoku, E.G., 2011. An algorithm for merging SMAP radiometer and radar data for high-resolution soil-moisture retrieval. IEEE Trans. Geosci. Remote Sens. 49, 1504–1512. https://doi.org/10.1109/TGRS.2010.2089526.

Das, N.N., Entekhabi, D., Member, S., Njoku, E.G., Shi, J.J.C., Member, S., Johnson, J.T., Colliander, A., Member, S., 2014. Tests of the SMAP combined radar and radiometer algorithm using airborne field campaign observations and simulated data. IEEE Trans. Geosci. Remote Sens. 52, 2018–2028. https://doi.org/10.1109/TGRS.2013.2257605.

De Rosnay, P., Drusch, M., Boone, A., Balsamo, G., Decharme, B., Harris, P., Kerr, Y., Pellarin, T., Polcher, J., Wigneron, J.P., 2009. AMMA land surface model intercomparison experiment coupled to the community microwave emission model: ALMIP-MEM. J. Geophys. Res. Atmos. 114, 1–18. https://doi.org/10.1029/2008JD010724.

Entekhabi, D., Njoku, E.G., O'Neill, P.E., Kellogg, K.H., Crow, W.T., Edelstein, W.N., Entin, J.K., Goodman, S.D., Jackson, T.J., Johnson, J., Kimball, J., Piepmeier, J.R., Koster, R.D., Martin, N., McDonald, K.C., Moghaddam, M., Moran, S., Reichle, R., Shi,

J.C., Spencer, M.W., Thurman, S.W., Tsang, L., Van Zyl, J., 2010. The soil moisture active passive (SMAP) mission. Proc. IEEE 98, 704–716. https://doi.org/10.1109/JPROC.2010.2043918.
Eom, H.J., Fung, A.K., 1984. A scatter model for vegetation up to Ku-band. Remote Sens. Environ. 15, 185–200.
Famiglietti, J.S., Ryu, D., Berg, A.A., Rodell, M., Jackson, T.J., 2008. Field observations of soil moisture variability across scales. Water Resour. Res. 44, 1–16. https://doi.org/10.1029/2006WR005804.
Fan, L., Wigneron, J.-P., Ciais, P., Chave, J., Brandt, M., Fensholt, R., Saatchi, S.S., Bastos, A., Al-Yaari, A., Hufkens, K., Qin, Y., Xiao, X., Chen, C., Myneni, R.B., Fernandez-Moran, R., Mialon, A., Rodriguez-Fernandez, N.J., Kerr, Y., Tian, F., Peñuelas, J., 2019. Satellite-observed pantropical carbon dynamics. Nat. Plants 5, 944–951. https://doi.org/10.1038/s41477-019-0478-9.
Franz, T.E., Zreda, M., Ferre, T.P.A., Rosolem, R., Zweck, C., Stillman, S., Zeng, X., Shuttleworth, W.J., 2012. Measurement depth of the cosmic ray soil moisture probe affected by hydrogen from various sources. Water Resour. Res. 48, 1–9. https://doi.org/10.1029/2012WR011871.
Gong, P., Wang, J., Yu, L., Zhao, Y., Zhao, Y., Liang, L., Niu, Z., Huang, X., Fu, H., Liu, S., Li, C., Li, X., Fu, W., Liu, C., Xu, Y., Wang, X., Cheng, Q., Hu, L., Yao, W., Zhang, H., Zhu, P., Zhao, Z., Zhang, H., Zheng, Y., Ji, L., Zhang, Y., Chen, H., Yan, A., Guo, J., Yu, L., Wang, L., Liu, X., Shi, T., Zhu, M., Chen, Y., Yang, G., Tang, P., Xu, B., Giri, C., Clinton, N., Zhu, Z., Chen, J., Chen, J., 2013. Finer resolution observation and monitoring of global land cover: first mapping results with Landsat TM and ETM+ data. Int. J. Remote Sens. 34, 2607–2654. https://doi.org/10.1080/01431161.2012.748992.
Holmes, T.R.H., Jackson, T.J., Reichle, R.H., Basara, J.B., 2012. An assessment of surface soil temperature products from numerical weather prediction models using ground-based measurements. Water Resour. Res. 48, 1–14. https://doi.org/10.1029/2011WR010538.
Holmes, T.R.H., Crow, W.T., Hain, C., Anderson, M.C., Kustas, W.P., 2015. Diurnal temperature cycle as observed by thermal infrared and microwave radiometers. Remote Sens. Environ. 158, 110–125. https://doi.org/10.1016/j.rse.2014.10.031.
Jackson, T.J., 1993. III. Measuring surface soil moisture using passive microwave remote sensing. Hydrol. Process. 7, 139–152.
Jackson, T.J., 1997. Soil moisture estimation using SSM/I satellite data over a grassland region. Water Resour. Res. 33, 1475–1484.
Jackson, T.J., Hsu, A.Y., 2001. Soil moisture and TRMM microwave imager relationships in the southern Great Plains 1999 (SGP99) experiment. IEEE Trans. Geosci. Remote Sens. 39, 1632–1642.
Jackson, T.J., Le Vine, D.M., Griffis, A.J., Goodrich, D.C., Schmugge, T.J., Swift, C.T., O'Neill, P.E., 1993. Soil moisture and rainfall estimation over a semiarid environment with the ESTAR microwave radiometer. IEEE Trans. Geosci. Remote Sens. 31, 836–841. https://doi.org/10.1109/36.239906.
Jackson, T.J., Engman, E.T., Le Vine, D., Schmugge, T.J., Lang, R., Wood, E., Teng, W., 1994. Multitemporal passive microwave mapping in Machydro'90. IEEE Trans. Geosci. Remote Sens. 32, 201–206. https://doi.org/10.1109/36.285203.
Jackson, T.J., Le Vine, D.M., Swift, C.T., Schmugge, T.J., Schiebe, F.R., 1995. Large area mapping of soil moisture using the ESTAR passive microwave radiometer in Washita'92. Remote Sens. Environ. 54, 27–37. https://doi.org/10.1016/0034-4257(95)00084-E.
Jackson, T.J., Le Vine, D.M., Hsu, A.Y., Oldak, A., Starks, P.J., Swift, C.T., Isham, J.D., Haken, M., 1999. Soil moisture mapping at regional scales using microwave radiometry: the southern Great Plains hydrology experiment. IEEE Trans. Geosci. Remote Sens. 37, 2136–2151. https://doi.org/10.1109/36.789610.
Jackson, T.J., Bindlish, R., Gasiewski, A.J., Stankov, B., Klein, M., Njoku, E.G., Bosch, D., Coleman, T.L., Laymon, C.A., Starks, P., 2005. Polarimetric scanning radiometer C- and X-band microwave observations during SMEX03. IEEE Trans. Geosci. Remote Sens. 43, 2418–2429. https://doi.org/10.1109/TGRS.2005.857625.
Jackson, T.J., Cosh, M.H., Bindlish, R., Member, S., Starks, P.J., Bosch, D.D., Seyfried, M., Goodrich, D.C., Moran, M.S., Member, S., Du, J., 2010. Validation of advanced microwave scanning radiometer soil moisture products. IEEE Trans. Geosci. Remote Sens. 48, 4256–4272.
Jackson, T.J., Bindlish, R., Cosh, M.H., Zhao, T., Starks, P.J., Bosch, D.D., Seyfried, M., Moran, M.S., Goodrich, D.C., Kerr, Y.H., Leroux, D., 2012. Validation of soil moisture and ocean salinity (SMOS) soil moisture over watershed networks in the U.S. IEEE Trans. Geosci. Remote Sens. 50, 1530–1543.
Jackson, T.J., Wigneron, J.P., Kerr, Y., Cosh, M., Colliander, A., Walker, J., Bindlish, R., 2016. Satellite-based soil moisture validation and field experiments: Skylab to SMAP. In: IEEE International Geoscience and Remote Sensing Symposium (IGARSS 2016), pp. 3462–3465.
Kerr, Y.H., Waldteufel, P., Wigneron, J.-P., Delwart, S., Cabot, F., Boutin, J., Escorihuela, M.-J., Font, J., Reul, N., Gruhier, C., Juglea, S.E., Drinkwater, M.R., Hahne, A., Martín-Neira, M., Mecklenburg, S., 2010. The SMOS Mission: new tool for monitoring key elements of the global water cycle. Proc. IEEE 98, 666–687. https://doi.org/10.1109/JPROC.2010.2043032.
Kerr, Y.H., Waldteufel, P., Richaume, P., Wigneron, J.P., Ferrazzoli, P., Mahmoodi, A., Al Bitar, A., Cabot, F., Gruhier, C., Juglea, S.E., Leroux, D., Mialon, A., Delwart, S., 2012. The SMOS soil moisture retrieval algorithm. IEEE Trans. Geosci. Remote Sens. 50, 1384–1403. https://doi.org/10.1109/TGRS.2012.2184548.
Kustas, W.P., Goodrich, D.C., 1994. Preface [to special section on Monsoon'90 multidisciplinary experiment]. Water Resour. Res. 30, 1211–1225.
Li, L., Gaiser, P.W., Gao, B.-C.G.B.-C., Bevilacqua, R.M., Jackson, T.J., Njoku, E.G., Rudiger, C., Calvet, J.-C., Bindlish, R., 2010. WindSat global soil moisture retrieval and validation. IEEE Trans. Geosci. Remote Sens. 48, 2224–2241. https://doi.org/10.1109/TGRS.2009.2037749.
Li, X., Cheng, G., Liu, S., Xiao, Q., Ma, M., Jin, R., Che, T., Liu, Q., Wang, W., Qi, Y., Wen, J., Li, H., Zhu, G., Guo, J., Ran, Y., Wang, S., Zhu, Z., Zhou, J., Hu, X., Xu, Z., 2013. Heihe watershed allied telemetry experimental research (HiWater) scientific objectives and experimental design. Bull. Am. Meteorol. Soc. 94, 1145–1160. https://doi.org/10.1175/BAMS-D-12-00154.1.
Li, X., Al-Yaari, A., Schwank, M., Fan, L., Frappart, F., Swenson, J., Wigneron, J.-P., 2020. Compared performances of SMOS-IC soil moisture and vegetation optical depth retrievals based on Tau-Omega and two-stream microwave emission models. Remote Sens. Environ. 236, 111502. https://doi.org/10.1016/J.RSE.2019.111502.
Li, Xin, Li, Xiaowen, Li, Z., Ma, M., Wang, Jian, Xiao, Q., Liu, Qiang, Che, T., Chen, E., Yan, G., Hu, Z., Zhang, L., Chu, R., Su, P., Liu, Qinhuo, Liu, S., Wang, Jindi, Niu, Z., Chen, Y., Jin, R., Wang, W., Ran, Y., Xin, X., Ren, H., 2009. Watershed allied telemetry experimental research. J. Geophys. Res. Atmos. 114, D22103. https://doi.org/10.1029/2008JD011590.
Magagi, R., Berg, A.A., Goita, K., Belair, S., Jackson, T.J., Toth, B., Walker, A., McNairn, H., O'Neill, P.E., Moghaddam, M., Gherboudj, I., Colliander, A., Cosh, M.H., Burgin, M., Fisher, J.B., Kim, S.B., Mladenova, I., Djamai, N., Rousseau, L.P.B., Belanger, J., Shang, J., Merzouki, A., 2013. Canadian experiment for soil moisture in 2010 (CanEx-SM10): overview and preliminary results. IEEE Trans. Geosci. Remote Sens. 51, 347–363. https://doi.org/10.1109/TGRS.2012.2198920.
McNairn, H., Jackson, T.J., Wiseman, G., Bélair, S., Berg, A., Bullock, P., Colliander, A., Cosh, M.H., Kim, S.B., Magagi, R., Moghaddam, M., Njoku, E.G., Adams, J.R., Homayouni, S., Ojo, E.R., Rowlandson, T.L., Shang, J., Goïta, K., Hosseini, M., 2015. The soil moisture active passive validation experiment 2012 (SMAPVEX12): prelaunch calibration and validation of the SMAP soil moisture algorithms. IEEE Trans. Geosci. Remote Sens. 53, 2784–2801. https://doi.org/10.1109/TGRS.2014.2364913.
McNairn, H., Jackson, T.J., Powers, J., Bélair, S., Berg, A., Bullock, P., Colliander, A., Cosh, M.H., Kim, S.B., Magagi, R., Pacheco, A., 2016. Experimental plan SMAP validation experiment 2016 in Manitoba, Canada (SMAPVEX16-MB). Available online at. https://smap.jpl.nasa.gov/internal_resources/390/.
Merlin, O., Walker, J.P., Kalma, J.D., Kim, E.J., Hacker, J., Panciera, R., Young, R., Summerell, G., Hornbuckle, J., Hafeez, M., Jackson, T., 2008. The NAFE06 data set: towards soil moisture retrieval at intermediate resolution. Adv. Water Resour. 31, 1444–1455. https://doi.org/10.1016/j.advwatres.2008.01.018.
Miller, M.A., et al., 2007. SGP Cloud and Land Surface Interaction Campaign (CLASIC): Science and Implementation Plan. Available online at. www.arm.gov/publications/programdocs/doe-sc-arm-0703.pdf.
Mironov, V.L., Dobson, M.C., Kaupp, V.H., Komarov, S.A., Kleshchenko, V.N., 2004. Generalized refractive mixing dielectric model for moist soils. IEEE Trans. Geosci. Remote Sens. 42, 773–785. https://doi.org/10.1109/TGRS.2003.823288.
Mo, T., Choudhury, B.J., Schmugge, T.J., Wang, J.R., Jackson, T.J., 1982. A model for microwave emission from vegetation-covered fields. J. Geophys. Res. Ocean 87, 11229–11237.
Narayan, U., Lakshmi, V., Njoku, E.G., 2004. Retrieval of soil moisture from passive and active L/S band sensor (PALS) observations during the soil moisture experiment in 2002 (SMEX02). Remote Sens. Environ. 92, 483–496. https://doi.org/10.1016/j.rse.2004.05.018.
Nichols, W.E., Cuenca, R.H., Schmugge, T.J., Wang, J.R., 1993. Pushbroom microwave radiometer results from HAPEX-MOBILHY. Remote Sens. Environ. 46, 119–128. https://doi.org/10.1016/0034-4257(93)90089-G.
Njoku, E.G., Chan, S.K., 2006. Vegetation and surface roughness effects on AMSR-E land observations. Remote Sens. Environ. 100, 190–199. https://doi.org/10.1016/j.rse.2005.10.017.
Njoku, E.G., Jackson, T.J., Lakshmi, V., Member, S., Chan, T.K., Nghiem, S. V, 2003. Soil moisture retrieval from AMSR-E. IEEE Trans. Geosci. Remote Sens. 41, 215–229.
O'Neill, P., Chan, S., Njoku, E., Jackson, T., Bindlish, R., 2018. Soil moisture active passive (SMAP) algorithm theoretical basis document: level 2 & 3 soil moisture (passive) data products. In: SMAP Project, JPL D-66480. Laboratory, Pasadena, CA, Jet Propulsion.
O'Neill, P., Chan, S., Njoku, E., Jackson, T., Bindlish, R., 2019. SMAP Enhanced L3 Radiometer Global Daily 9 km EASE-Grid Soil Moisture, Version 3. Boulder, Colorado USA. NASA National Snow and Ice Data Center Distributed Active Archive Center. https://doi.org/10.5067/T90W6VRLCBHI.
Owe, M., de Jeu, R., Holmes, T., 2008. Multisensor historical climatology of satellite-derived global land surface moisture. J. Geophys. Res. Earth Surf. 113, 1–17. https://doi.org/10.1029/2007JF000769.
Paloscia, S., Macelloni, G., Santi, E., 2006. Soil moisture estimates from AMSR-E brightness temperatures by using a dual-frequency algorithm. IEEE Trans. Geosci. Remote Sens. 44, 3135–3144.
Panciera, R., Walker, J.P., Kalma, J.D., Kim, E.J., Hacker, J.M., Merlin, O., Berger, M., Skou, N., 2008. The NAFE'05/CoSMOS data set: toward SMOS soil moisture retrieval, downscaling, and assimilation. IEEE Trans. Geosci. Remote Sens. 46, 736–745. https://doi.org/10.1109/TGRS.2007.915403.
Panciera, R., Walker, J.P., Jackson, T.J., Gray, D.A., Tanase, M.A., Ryu, D., Monerris, A., Yardley, H., Rüdiger, C., Wu, X., Gao, Y., Hacker, J.M., 2014. SMAPEx: toward soil moisture retrieval from the SMAP mission. IEEE Trans. Geosci. Remote Sens. 52, 490–507.
Pardé, M., Zribi, M., Wigneron, J.P., Dechambre, M., Fanise, P., Kerr, Y., Crapeau, M., Saleh, K., Calvet, J.C., Albergel, C., Mialon, A., Novello, N., 2011a. Soil moisture estimations based on airborne CAROLS L-band microwave data. Remote Sens. 3, 2591–2604. https://doi.org/10.3390/rs3122591.
Pardé, M., Zribi, M., Fanise, P., Dechambre, M., 2011b. Analysis of RFI issue using the CAROLS L-band experiment. IEEE Trans. Geosci. Remote Sens. 49, 1063–1070. https://doi.org/10.1109/TGRS.2010.2069101.
Peischl, S., Walker, J.P., Rüdiger, C., Ye, N., Kerr, Y.H., Kim, E., Bandara, R., Allahmoradi, M., 2012. The AACES field experiments: SMOS calibration and validation across the Murrumbidgee River catchment. Hydrol. Earth Syst. Sci. 16, 1697–1708. https://doi.

org/10.5194/hess-16-1697-2012.
Robinson, D.A., Campbell, C.S., Hopmans, J.W., Hornbuckle, B.K., Jones, S.B., Knight, R., Ogden, F., Selker, J., Wendroth, O., 2008. Soil moisture measurement for ecological and hydrological watershed-scale observatories: a review. Vadose Zo. J. 7, 358. https://doi.org/10.2136/vzj2007.0143.
Saini, R., Wang, G., Pal, J.S., 2016. Role of soil moisture feedback in the development of extreme summer drought and flood in the United States. J. Hydrometeorol. 17, 2191–2207. https://doi.org/10.1175/jhm-d-15-0168.1.
Saleh, K., Wigneron, J.P., Calvet, J.C., Lopez-Baeza, E., Ferrazzoli, P., Berger, M., Wursteisen, P., Simmonds, L., Miller, J., 2004. The EuroSTARRS airborne campaign in support of the SMOS mission: first results over land surfaces. Int. J. Remote Sens. 25, 177–194. https://doi.org/10.1080/0143116031000116444.
Schmugge, T., Jackson, T.J., Kustas, W.P., Wang, J.R., 1992. Passive microwave remote sensing of soil moisture: results from HAPEX, FIFE and MONSOON 90. ISPRS J. Photogramm. Remote Sens. 47, 127–143.
Seneviratne, S.I., Corti, T., Davin, E.L., Hirschi, M., Jaeger, E.B., Lehner, I., Orlowsky, B., Teuling, A.J., 2010. Investigating soil moisture-climate interactions in a changing climate: a review. Earth Sci. Rev. 99, 125–161. https://doi.org/10.1016/j.earscirev.2010.02.004.
Shi, J., Wang, J., Hsu, A.Y., O'Neill, P.E., Engman, E.T., 1997. Estimation of bare surface soil moisture and surface roughness parameter using L-band SAR image data. IEEE Trans. Geosci. Remote Sens. 35, 1254–1266. https://doi.org/10.1109/36.628792.
Shi, J., Dong, X., Zhao, T., Du, J., Jiang, L., Du, Y., Liu, H., Wang, Z., Ji, D., Xiong, C., 2014. WCOM: the science scenario and objectives of a global water cycle observation mission. In: IEEE International Geoscience and Remote Sensing Symposium (IGARSS 2016), pp. 3646–3649.
Tabatabaeenejad, A., Burgin, M., Duan, X., Moghaddam, M., 2015. P-band radar retrieval of subsurface soil moisture profile as a second-order polynomial: first AirMOSS results. IEEE Trans. Geosci. Remote Sens. 53, 645–658. https://doi.org/10.1109/TGRS.2014.2326839.
Teuling, A.J., Troch, P.A., 2005. Improved understanding of soil moisture variability dynamics. Geophys. Res. Lett. 32, 1–4. https://doi.org/10.1029/2004GL021935.
Topp, C., 1980. Electromagnetic determination of soil water content. Water Resour. Res. 16, 574–582.
Wang, J.R., Shiue, J.C., Schmugge, T.J., Engman, E.T., 1990. The L-band PBMR measurements of surface soil moisture in FIFE. IEEE Trans. Geosci. Remote Sens. 28, 906–914. https://doi.org/10.1109/36.58980.
Vereecken, H., Huisman, J.A., Bogena, H., Vanderborght, J., Vrugt, J.A., Hopmans, J.W., 2008. On the value of soil moisture measurements in vadose zone hydrology: a review. Water Resour. Res. 46, 1–21. https://doi.org/10.1029/2008WR006829.
Wang, J.R., Hsu, A., Shi, J.C., O'Neill, P.E., Engman, E.T., 1997. A comparison with soil moisture retrieval models using SIR-C measurements over the Little Washita River watershed. Remote Sens. Environ. 59, 308–320. https://doi.org/10.1016/S0034-4257(96)00145-9.
Wigneron, J.P., Calvet, J.C., Pellarin, T., Van De Griend, A.A., Berger, M., Ferrazzoli, P., 2003. Retrieving near-surface soil moisture from microwave radiometric observations: current status and future plans. Remote Sens. Environ. 85, 489–506. https://doi.org/10.1016/S0034-4257(03)00051-8.
Wigneron, J.P., Member, S., Pardé, M., Waldteufel, P., Chanzy, A., Kerr, Y., Member, S., Schmidl, S., Skou, N., 2004. Characterizing the Dependence of Vegetation Model Parameters on Crop Structure. Incidence Angle, and Polarization at L-Band 42, 416–425.
Wigneron, J.P., Kerr, Y., Waldteufel, P., Saleh, K., Escorihuela, M.J., Richaume, P., Ferrazzoli, P., de Rosnay, P., Gurney, R., Calvet, J.C., Grant, J.P., Guglielmetti, M., Hornbuckle, B., Mätzler, C., Pellarin, T., Schwank, M., 2007. L-band microwave emission of the biosphere (L-MEB) model: description and calibration against experimental data sets over crop fields. Remote Sens. Environ. 107, 639–655. https://doi.org/10.1016/j.rse.2006.10.014.
Wigneron, J.P., Jackson, T.J., O'Neill, P., De Lannoy, G., de Rosnay, P., Walker, J.P., Ferrazzoli, P., Mironov, V., Bircher, S., Grant, J.P., Kurum, M., Schwank, M., Munoz-Sabater, J., Das, N., Royer, A., Al-Yaari, A., Al Bitar, A., Fernandez-Moran, R., Lawrence, H., Mialon, A., Parrens, M., Richaume, P., Delwart, S., Kerr, Y., 2017. Modelling the passive microwave signature from land surfaces: a review of recent results and application to the L-band SMOS & SMAP soil moisture retrieval algorithms. Remote Sens. Environ. https://doi.org/10.1016/j.rse.2017.01.024.
Zarlenga, A., Fiori, A., Russo, D., 2018. Spatial variability of soil moisture and the scale issue: a geostatistical approach. Water Resour. Res. 54, 1765–1780.
Zhang, T., Jiang, L., Chai, L., Zhao, T., Wang, Q., 2015. Estimating mixed-pixel component soil moisture contents using biangular observations from the HiWATER airborne passive microwave data. IEEE Geosci. Remote Sens. Lett. 12, 1146–1150. https://doi.org/10.1109/LGRS.2015.2388572.
Zhao, T., Shi, J., Bindlish, R., Jackson, T., Cosh, M., Jiang, L., Zhang, Z., Lan, H., 2015. Parametric exponentially correlated surface emission model for L-band passive microwave soil moisture retrieval. Phys. Chem. Earth 83–84, 65–74.
Zribi, M., Pardé, M., Boutin, J., Fanise, P., Hauser, D., Dechambre, M., Kerr, Y., Leduc-Leballeur, M., Reverdin, G., Skou, N., Soøbjærg, S., Albergel, C., Calvet, J.C., Wigneron, J.P., Lopez-Baeza, E., Rius, A., Tenerelli, J., 2011. CAROLS: a new airborne L-band radiometer for ocean surface and land observations. Sensors 11, 719–742. https://doi.org/10.3390/s110100719.